Zn₂MnSbO₆ and Zn₂FeSbO₆: Two New Polar High-Pressure Ordered Corundum-Type Compounds

Published as part of Chemistry of Materials special issue "In Memory of Prof. Francis DiSalvo".

Alessia Provino, Thomas J. Emge, David Walker, Corey E. Frank, Suguru Yoshida, Venkatraman Gopalan, Mark Croft, Zheng Deng, Changqing Jin, Pietro Manfrinetti, and Martha Greenblatt*

Cite This: https://doi.org/10.1021/acs.chemmater.4c02146

Read Online

ACCESS | Metrics & More | Article Recommendations | SI Supporting Information

ABSTRACT: Two new compounds, Zn_2FeSbO_6 and Zn_2MnSbO_6, have been synthesized under high-pressure and high-temperature conditions. The synthesis, single-crystal and powder X-ray diffraction, X-ray absorption near-edge spectroscopy (XANES), optical second harmonic generation (SHG), and magnetic and heat capacity measurements were carried out for both compounds and are described. The lattice parameters are $a = 5.17754(6)$ Å and $c = 13.80045(16)$ Å for Zn_2FeSbO_6 and $a = 5.1889(10)$ Å and $c = 14.0418(3)$ Å for Zn_2MnSbO_6. Single-crystal X-ray diffraction analyses indicate that Zn_2FeSbO_6 consists of a cocrystal of superimposed Ni_3TeO_6 (NTO) and ordered ilmenite (OIL) components with a ratio of approximately 2:1 and Zn_2MnSbO_6 contains two nearly identical, but noncrystallographically related, OIL components in a ratio of approximately 6:1. XANES analysis shows Fe^{3+} and Mn^{3+} as formal oxidation states for Fe and Mn cations, respectively, for these $A_2BB'O_6$ compounds. SHG measurements for Zn_2MnSbO_6 indicate that it is noncentrosymmetric and confirm the polar $R3$ (no. 146) space group strongly implied by single-crystal reflection data. The magnetic measurements reveal spin-glass behavior with antiferromagnetic (AFM) interactions in both compounds and a frustration factor (f) being significantly larger for Zn_2MnSbO_6 ($f \approx 20$) compared to Zn_2FeSbO_6 ($f \approx 7$). While Zn_2FeSbO_6 exhibits AFM ordering at a Néel temperature (T_N) of 9 K, Zn_2MnSbO_6 shows magnetic ordering around 4 K. Additionally, the negative Curie–Weiss temperatures for both compounds corroborate the presence of AFM exchange interactions.
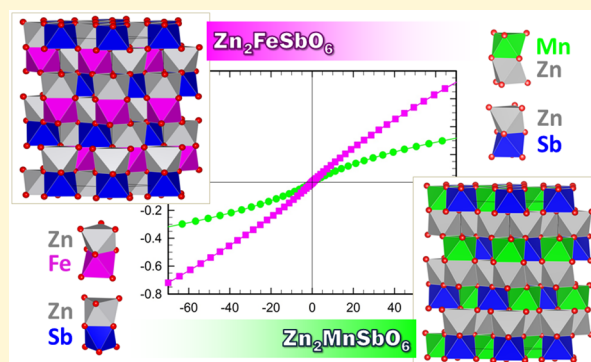
1. INTRODUCTION

In the ever-evolving field of materials science, transition metal double perovskites (DPs) $A_2BB'O_6$ (where A, B, and B' are different cations) stand out as an intriguing and versatile class of compounds that has captured the interest of researchers worldwide in the pursuit of innovative materials with tailored properties.[1−7] Since then, several DPs have been reported and among them are Sr_2FeReO_6 and Sr_2FeMoO_6, the latter showing room temperature (RT) colossal magnetoresistance.[8−10]

In contrast to the simple cubic perovskite ABO_3, DPs differ by incorporating two distinct B and B' transition metal cations within the crystal lattice. This dual inclusion gives rise to distinctive crystal and electronic structures which, jointly with a flexible choice of chemical composition, make them an almost limitless source of novel materials showcasing a multitude of interesting physical properties such as multiferroicity, ferroelectricity, colossal magnetoresistance, thermoelectricity, piezoelectricity, superconductivity, metallic, half-

metallic, and insulating behaviors, second harmonic generation (SHG) effect, ionic conductivity, catalytic properties, high thermopower, and several magnetic properties such as ferromagnetism (FM), antiferromagnetism (AFM), and ferrimagnetism (FIM).[11−22] While the crystal structure of the simple cubic ABO_3 consists of corner-sharing BO_6 octahedra extending by translational symmetry in three dimensions (3D) and of 12-fold coordinated A cations filling the cavities created by the BO_6 octahedra, the DP structure is similar to ABO_3 with respect to ordering of the B/B' cations usually on alternate octahedral sites and rarely in a layered arrangement. This structural feature is responsible for the extraordinary physical

Table 1. Comparative List of Crystallographic Information for Most of the Determined Structures of NTO-like Phases[69]

formula	c/a	sample type	radiation	reference
$Co_{0.5}Ni_{1.5}Sc[SbO_6]$	2.705	powder	neutrons	[49]
$Co_{1.5}Ni_{0.5}Sc[SbO_6]$	2.688	powder	neutrons	[49]
$Co_2Sc[SbO_6]$	2.682	powder	neutrons	[49]
$CoNiSc[SbO_6]$	2.698	powder	neutrons	[49]
$Ni_2Sc[SbO_6]$	2.711	powder	neutrons	[49]
$Co_{1.5}Mn_{1.5}[TeO_6]$	2.625	powder	synchrotron and neutron	[50]
$Co_{0.5}Mn_{2.5}[TeO_6]$	2.653	powder	synchrotron	[50]
$Co_3[TeO_6]$	2.661	powder	neutrons	[50]
$Co_{1.5}Ni_{1.5}[TeO_6]$	2.682	powder	neutrons	[51]
$Co_{1.5}Ni_{1.5}[TeO_6]$	2.692	powder	neutrons	[51]
$Co_3[TeO_6]$	2.662	single crystal	X-rays, Mo Kα1	[52]
$FeBi_2AlO_6$	2.494	powder	neutrons	[53]
$La_2Mg[GeO_6]$	2.418	powder	neutrons	[54]
$Li_{0.1}Mg_{2.8}Mn_{0.1}[TeO_6]$	2.686	powder	synchrotron	[68]
$Li_{1.75}Zr_{0.75}Nb_{0.25}[TeO_6]$	2.67	powder	X-rays, Cu Kα	[55]
$Li_2Zr[TeO_6]$	2.677	powder	X-rays, Cu Kα	[55]
$Li_2Ge[TeO_6]$	2.863	powder	X-rays, Cu Kα	[56]
$Li_2Ge[TeO_6]$	2.864	powder	synchrotron	[25]
$Li_2Hf[TeO_6]$	2.669	powder	X-rays, Cu Kα	[27]
$Li_2Zr[TeO_6]$	2.677	powder	X-rays, Cu Kα	[27]
$Li_2Zr[TeO_6]$	2.678	single crystal	X-rays, Mo Kα	[57]
$Mg_3[TeO_6]$	2.687	single crystal	X-rays, Mo Kα	[58]
$Mn_2Fe[MoO_6]$	2.633	powder	neutrons	[74]
$Mn_2Fe[MoO_6]$, high-T phase	2.736	powder	neutrons	[74]
$Mn_2Fe[WO_6]$	2.632	powder	synchrotron	[14]
$Mn_2In[SbO_6]$	2.64	powder	neutrons	[59]
$Mn_2Sc[NbO_6]$	2.662	powder	synchrotron	[18]
$Mn_2Sc[TaO_6]$	2.659	powder	synchrotron	[18]
$Mn_2Sc[SbO_6]$	2.632	powder	neutrons	[60]
$Mn_3[SbO_6]$	2.711	powder	synchrotron	[20]
$Mn_3[WO_6]$	2.641	powder	synchrotron	[48]
$Ni_{1.5}Co_{1.5}[TeO_6]$	2.69	powder	X-rays, Cu Kα	[61]
$Ni_{2.5}Co_{0.5}[TeO_6]$	2.695	powder	X-rays, Cu Kα	[61]
$Ni_{2.5}Mg_{0.5}[TeO_6]$	2.697	powder	X-rays, Cu Kα	[61]
$Ni_{2.5}Mn_{0.5}[TeO_6]$	2.702	powder	X-rays, Cu Kα	[61]
$Ni_{2.1}Mn_{0.9}[TeO_6]$	2.71	powder	neutrons	[62]
$Ni_{2.5}Mn_{0.5}[TeO_6]$	2.703	powder	X-rays, Cu Kα	[62]
$Ni_{2.5}Mn_{0.5}[TeO_6]$	2.708	single crystal	X-rays, Mo Kα	[62]
$Ni_2In[SbO_6]$	2.687	twinned crystal	X-rays, Mo Kα	[63]
$Ni_2In[SbO_6]$	2.687	powder	neutrons	[30]
$Ni_2In[SbO_6]$	2.687	powder	X-rays, Cu Kα1	[30]
$Ni_2In[SbO_6]$	2.688	powder	neutrons	[30]
$Ni_2Sc[SbO_6]$	2.711	powder	neutrons	[30]
$Ni_2Sc[SbO_6]$	2.711	powder	X-rays, Cu Kα1	[30]
$Ni_2Sc[SbO_6]$	2.713	powder	neutrons	[30]
$Ni_3[TeO_6]$	2.695	powder	X-rays, Cu Kα1	[30]
$Ni_2Mn[TeO_6]$	2.71	powder	neutrons	[64]
$Ni_2Mn[TeO_6]$	2.712	powder	neutrons	[64]
$Ni_3[TeO_6]$	2.695	single crystal	X-rays, Mo Kα	[65]
$Ni_3[TeO_6]$	2.695	powder	X-rays, Cu Kα	[66]
$Ni_3[TeO_6]$	2.695	powder	synchrotron	[67]
$Ni_3[TeO_6]$	2.697	powder	synchrotron	[67]

properties typical of perovskite compounds. Depending on the size and charge of A and B cations,[1,15,23] as well as the synthesis conditions such as high pressures and high temperatures, the formation of new phases can be induced by not only the choice of cations but also by altering the atomic arrangement and crystal structure. Properties have been tailored by manipulating the highly flexible chemical composition of A and B cations and by applying a high pressure and high temperature during synthesis.[23−27]

The stability of ABO_3 or $A_2BB'O_6$ perovskite and related structures can be roughly predicted by the Goldschmidt tolerance factor, t {where t is defined as $t = (r_A + r_O)/\sqrt{2}\ (r_B + r_O)$, where r_A, r_B, and r_O are the ionic radii of the A, B/B′, and O ions[24]}. If $t = 0.9$ to 1.0, where the A and B/B′ cations have

an ideal size, a "perfect" cubic perovskite crystallizing in the $SrTiO_3$ phase type ($cP5$, Pm-$3m$, no. 221) is possible. However, in most cases, the symmetry is lower than cubic. For $t > 1$, where the A cations are large or B/B′ cations are small, the hexagonal $BaNiO_3$ phase type ($hP10$, $P6_3/mmc$, no. 194) is adopted; for $t = 0.85$−0.9, where the A cations are much smaller than B/B′, the orthorhombic $GdFeO_3$ type ($oP20$, $Pnma$, no. 62) is formed; and for $t < 0.85$, where the A and B cations are comparable in size, a rhombohedral crystal structure typical of either the $LiNbO_3$-type ($hR30$, $R3c$, no. 161) (LN), or $TiFeO_3$-type ($hR30$, R-3, no, 148) (Ilmenite, IL), or Ni_3TeO_6-type ($hR30$, $R3$, no. 146) (NTO) is observed. Therefore, depending on the relative size of A and B cations and on temperature and pressure synthesis conditions, while the chemical formula ABO_3 or $A_2BB'O_6$ remains, the structure and symmetry can vary dramatically. The BO_6 and $B'O_6$ octahedra can undergo distortions such as elongation or contraction (similar to Jahn−Teller distortion) and/or tilting, and the A-cation site can shift from its ideal position into two or more different Wyckoff sites, giving rise to several possible structural prototypes. Among them, the cubic perovskite $SrTiO_3$-type is nonpolar (NP) centrosymmetric (CS) with A and B cations occupying the $1b$ and $1a$ Wyckoff sites, respectively (with A larger than B), and O anions the $3d$ site. The hexagonal $BaNiO_3$ type is NP-CS, and A and B cations fill two sites with symmetry $2d$ and $2a$, respectively, while the O anions occupy the $6h$ site. The orthorhombic $GdFeO_3$ type is NP-CS, and A and B occupy two sites with symmetry $4c$ and $4a$ sites, respectively, while the O anions occupy another $4c$ site and a $8d$ site. The rhombohedral $LiNbO_3$ type (LN) is polar (P) noncentrosymmetric (NCS), and A and B cations occupy two different crystallographically ordered $6a$ sites, while O anions fill the $18b$ site. The rhombohedral $TiFeO_3$ type is NP-CS, and A and B cations statistically occupy two different $6c$ sites, while O anions occupy the $18f$ site. The rhombohedral Ni_3TeO_6 type (Ni_2NiTeO_6) is P-NCS, and A and B cations occupy four different $3c$ Wyckoff sites (two $3c$ sites are generally occupied by A cations and two $3c$ sites are typically filled by B cations), while O anions fill two sites with $9b$ symmetry.

The P or NCS phases with corundum-based structures, LN and NTO types, whose crystal structure lacks symmetry operations that cancel dipole moments and result in a nonzero electric dipole moment, are of great interest due to their symmetry-dependent properties, i.e., multiferroicity, piezo-electricity, ferroelectricity, spintronics, and SHG effect. The design and synthesis of these corundum-based structures is not an easy task due the fact that the NP-CS perovskites tend to be more thermodynamically stable than the P-NCS ones. The formation of P-NCS corundum-type LN and NTO phases with small transition metal (T) cations may be stabilized and their synthesis favored but only under extreme synthesis conditions of high pressures and high temperatures (HPHT).[13,28−30] Corundum-type phases with T cations at both the A and B/B′ sites continue to attract significant attention because of their potentially useful physical properties.[10,31−42] Among the $A_2BB'O_6$ corundum-type phases prepared under HPHT reported in the literature are the LN-type P-NCS Mn_2FeNbO_6 and Mn_2FeTaO_6 (both prepared under $P = 7$ GPa and at $T = 1573$ K),[13] the NTO-type P-NCS Mn_2FeWO_6 and Mn_2FeMoO_6 (both prepared under $P = 8$ GPa and at $T = 1623$ K),[14,43] the IL-type NP-CS Mn_2BSbO_6 (B = Fe, V, Cr, Ga, Al) (prepared between $P = 3$−9 GPa and $T = 700$−1000

°C).[44] Among these, Mn_2FeSbO_6 is a ferrimagnet at $T_C = 270$ K[45] and Zn_2FeTaO_6 orders antiferromagnetically at $T_N \approx 22$ K.[46] While an antiferromagnetic transition in Zn_2FeOsO_6 was only theoretically predicted,[47] Mn_2MnWO_6 does transform to an antiferromagnet at $T = 58$ K,[48] and Mn_2MnMoO_6 shows two antiferromagnetic transitions at $T_{N1} = 47$ K and $T_{N2} = 19$ K.[21]

During our search to discover new corundum-based phases that form under HPHT conditions, we successfully synthesized the two new compounds Zn_2FeSbO_6 and Zn_2MnSbO_6, which are the first compounds of this type to contain Zn^{2+} cations. In this work, we have investigated the crystal structure and symmetry of cation octahedra, magnetic properties, heat capacity, SHG, and the oxidation states of Fe and Mn. Additionally, we have elucidated the essential relationships between the crystal structures, symmetries, and magnetic properties of these two new compounds.

1.1. Problem of Twinning in NTO-like Phases and Implications for Their Crystallographic Characterization.

The single-crystal reflection data for Zn_2FeSbO_6 (sample TT1375) and Zn_2FeSbO_6 (sample TT1478) were found to have the P-NCS rhombohedral symmetry, which is observed for many Ni_3TeO_6-like (NTO) phases including Li_2ZrTeO_6-like (LZTO) and Li_2GeTeO_6-like (e.g., ordered ilmenite, OIL) phases.[14,15,18,20,25,27,30,48−68] As a broader class of materials with only minor structural differences between prototypes (as evidenced by similar powder X-ray diffraction patterns), all these types of $A_2BB'O_6$ compounds will herein be referred to as NTO-like phases. A comparative list of crystallographic information for most of the determined structures of NTO-like phases is presented in Table 1.[69] Unlike powder X-ray diffraction (PXRD) profile data, reflection data from single-crystal data (SCD) can be used to precisely determine not only the contributions from all diffraction domains but also any multiple structural (e.g., cocrystal) components.[70,71] However, to date, there are only six SCD studies of NTO-like phases, and all of them unfortunately have used relatively low-resolution Mo Kα X-ray data. Namely, the SCD results for Li_2ZrTeO_6 and $Ni_{3−x}Mn_xTeO_6$ have data with $\theta_{max} < 30°$,[57,62] Ni_3TeO_6, Co_3TeO_6, and Mg_3TeO_6 have data with $\theta_{max} < 40°$[52,58,65] and Ni_2InSbO_6 has data with $\theta_{max} = 46°$,[63] even though all diffractometers used were capable of resolutions much better than $\theta_{max} = 70°$. Based upon our experience with dozens of samples, this shortcoming is often due to multiple component issues (e.g., twinning and especially multigrowth) and especially to long-range order issues (e.g., crystallinity or mosaicity). These difficulties may be the result of extreme synthesis conditions, namely, a high pressure and temperature followed by relatively quick cooling, which may be magnified due to internal stresses within the lattice resulting from incompatible sizes or electronic configurations of the cations used.[1,15,72] In the SCD study of Ni_2InSbO_6, whose synthesis involved a long annealing time (2 weeks), large single crystals of acceptable mosaicity were obtained; nevertheless, such crystals were twinned.[63] The derived model in that study did not contain any cation site mixing. Such a result, namely, all sites having a single, ordered atom type, is not the case for nearly all of the other known powder diffraction studies of NTO, LZTO, or OIL phases, where different cations were used for the A and B site (see Table 1). For three of the six SCD studies mentioned above, an M_3TeO_6 phase with only one divalent transition metal present (M = Co, Mg, Ni) for both A and B sites was used. A fifth study concerned

Li_2ZrTeO_6,[57] which is also a phase containing all ordered cation sites and an occupation preference for the A or B site dependent upon the different ionization potentials rather than ionic radius of Li (0.76 Å) versus Zr (0.72 Å). For that SCD study, the large atomic number difference between Li (Z = 3) and Zr (Z = 40) made it quite easy to obtain accurate PXRD and SCD results. The sixth SCD study mentioned above concerned a completely ordered Ni_2InSbO_6 phase[63] with reflection data of high enough resolution ($\theta_{max} = 46°$) to refine anisotropic atomic displacement parameters (ADP), but these are not reported in that study. Additionally, although an absolute structure parameter from the SHELXL refinement program has been reported, none of these studies have a discussion of the problems of crystal intergrowth or the crucial role of quantifying all twinning contributions. Twinning may be due to nonmerohedral twinning (e.g., crystal intergrowth with nonoverlapping rotational components), twinning by merohedry (e.g., racemic mixing for chiral compounds), and twinning by reticular merohedry (e.g., obverse/reverse twinning). This is especially important since data collected for a sample with the last two types of twinning have an exact overlap of reflections having individually different indices and intensities, a situation that exists for all lattice points. Thus, these types of twinning can greatly complicate the solution or refinement of a crystal structure. For most of the dozens of samples of Zn_2MSbO_6 with M = Fe or Mn, and all other NTO-type phases that we have examined by use of the SCD diffractometer, we have found all three types of twinning to be present. For this study, we have chosen single-crystal samples without significant nonmerohedral twinning by simple examination of reciprocal lattice plots and rejecting crystals containing two or more offset lattices of reflections. Twinning by merohedry and reticular merohedry appeared to always be present in our samples and in different ratios for different single-crystal samples. Twinning of this sort may be expected based on the rate of change from HPHT to ambient conditions during the final steps of the synthesis. It is also likely that twinning can be generated in the initial nucleation and growth of the polar corundum derivatives (PCD) from oxide mixtures. Spontaneous resolution of chiral crystals was not expected, but we and others have observed very low racemic ratios.[52,57,58,62,63,65] One study had found that annealing samples over periods of weeks seemed to produce less, but not zero, twinning.[30] It is unknown if reticular merohedry (obverse/reverse twinning) was ever accounted for in that study or any other single-crystal study to date.

The 3D framework of the O anions defines this class of PCDs by means of characteristic face sharing and tilting of the O6 octahedra. In contrast to the common occurrence of cation disorder, the O6 octahedra appear to be ordered for all known structures, and as a framework, they serve as the anchor for all structures of NTO-like phases. Deficiencies in O anion sites have been predicted for cubic and ilmenite perovskite-related phases[73] but not quantified in any SCD study of NTO-like compounds, including both compounds in this study. Additionally, O anion disorder is not observed or is negligible, and only U_{iso} values of 0.02 Å^2 or less have been found in our studies or in published single-crystal results. For determining precise positional and displacement parameters of the relatively lighter O anions in the crystal structures of NTO-like phases, the diffraction of neutrons is generally preferred to X-rays, and 13 of the 29 structure determinations summarized in Table 1 are based upon neutron powder diffraction (NPD). For the

PXRD studies listed in Table 1, six of them employed high-resolution synchrotron X-rays, and four studies used lower-resolution data from in-house Cu Kα X-ray sources ($\theta_{max} = 60°$). Nevertheless, examination of bulk materials by the PXRD method is always essential for identifying crystal symmetry and phase purity of the sample before quantitative results (e.g., Rietveld) can be reliably obtained. The real value of using SCD data for structure refinements of PCDs is the determination of accurate composition and coordination geometry of all sites, and especially mixed-atom sites. The high correlations between occupancy and anisotropic displacement can best be accommodated with high-resolution single-crystal data. Obtaining the high-resolution data is, of course, dependent on sample mosaicity, and the necessary triage to find such a sample may take numerous attempts. Unfortunately, the ADP derived from powder diffraction data is, in general, poorly determined or even ignored. Lack of complete profile shapes, usually because of the choice of slits or use of the divergent X-ray sources from sealed tubes, requires the use of averaged values (U_{iso} or B_{iso}) for powder samples. For the SCD experiment, only after accurate determination of the number and contribution of all domains within the sample can reliable ADP values be obtained. Thus, it is of great advantage to use single crystals of high purity and a single domain. However, the process of selecting a sample of adequate crystallinity, especially for deeply colored samples (as are most NTO-like samples), is often random and time-consuming. To date, there are no studies that examine the distribution of phase or degree of crystallinity of individual particles/grains from any type of synthesis (e.g., HT or HTHP). For PXRD and NPD studies, the crystal structure of individual particles is assumed to be the same as the average structure of a bulk region, within boundaries selected by the use of microscopic or spectroscopic methods. This assumption is often made even though one study has shown a cation site rearrangement at a high temperature.[74]

The framework of the O anions in NTO-like structures has been shown to be consistent and to contain well-ordered O anions in all structure determinations (e.g., this study and those in Table 1). Thus, conclusions about cation size and cation–cation interactions forming the basis of observed octahedral distortions and resulting physical properties are generally correct. This relationship is supported by the fact that all NTO-like structures reside in space group $R3$ with similar face sharing and tilts of the O6 octahedra, especially with respect to the crystallographic c-axis as listed in Table 1. This consistency in observations is also independent of the temperature and type of radiation used. For NTO-like phases, the enclosed volume of the O6 octahedra does not appear to be limiting for cations of ionic radius of 0.6 Å or less. When Li$^+$ or Mg^{2+} atoms are used in the A sites, an OIL-like phase rather than an NTO-like phase usually forms,[25,27,55−58,68] indicating an influence of ion potential upon the selection and location of cation sites. For all NTO-like structures, adjacent face-sharing octahedra have metal positions displaced from the symmetrical centroid and away from each other such that the shortest theoretical cation-to-cation distance of about 2.30 Å is never achieved for any A-A, A-B, A-B′, or B-B′ distance between face-sharing octahedra, as indicated by the range of values 2.75−3.5 Å for the NTO, OIL, and LZTO phases in Table 1. Thus, the observed site selection and distortions of metal coordination geometry are likely due to short-range repulsive cation−cation interactions within adjacent face-shared octahe-

Table 2. Single-Crystal Data and Refinement Details for Zn_2FeSbO_6 and Zn_2MnSbO_6

| compound	Zn_2FeSbO_6	Zn_2MnSbO_6
sample ID	TT1375	TT1478
empirical formula	Zn_2FeSbO_6	Zn_2MnSbO_6
formula weight	404.34 g/mol	403.43 g/mol
structural prototype	Ni_3TeO_6	Ni_3TeO_6
Pearson code	$hR30$	$hR30$
crystal system	trigonal	trigonal
space group	$R3$ (No. 146)	$R3$ (No. 146)
lattice parameters	a = 5.17754(6) Å	a = 5.1889(10) Å
	c = 13.80045(16) Å	c = 14.0418(3) Å
unit cell volume	320.384(9) Å^3	327.419(14) Å^3
unit formula per cell, Z	3	3
calculated density, ρ	6.287 g/cm^3	6.138 mg/m^3
absorption coefficient, μ	20.624 mm^{-1}	19.750 mm^{-1}
$F(000)$	555	552
data collection temperature	293(2) K	298(2) K
crystal description	black block	black block
crystal size	0.056 × 0.046 × 0.035 mm^3	0.054 × 0.048 × 0.020 mm^3
theta range collected (after cutoff)	4.431° ≤ ϑ ≤ 79.67° (65.67°)	4.354° ≤ ϑ ≤ 79.76° (64.11°)
index ranges h, k, l (after cutoff)	−13 ≤ h ≤ 11	−13 ≤ h ≤ 13
	−13 ≤ k ≤ 13	−13 ≤ k ≤ 9
	−36 ≤ l ≤ 35	−35 ≤ l ≤ 35
reflections collected	17,909	7641
independent reflections	16,436	7418
resolution cutoff used	0.39 Å	0.395 Å
R_{int}	0.0374	0.0282
completeness to theta = 25.242°	99.2%	99.2%
absorption correction	Gaussian	Gaussian
maximal and minimal transmission	0.748 and 0.568	0.971 and 0.776
refinement method	full-matrix least-squares on F^2	full-matrix least-squares on F^2
data/restraints/parameter	2512/30/44	2473/60/43
goodness of fit on F^2	1.018	1.018
final R indices $[I > 2\sigma(I)]$	$R1$ = 0.0156, $wR2$ = 0.0365	$R1$ = 0.0308, $wR2$ = 0.0803
R indices (all data)	$R1$ = 0.0156, $wR2$ = 0.0365	$R1$ = 0.0311, $wR2$ = 0.0803
absolute structure parameter	0.48(2)	0.17(4)
extinction coefficient	0.0072(4)	0.0009(8)
largest diff. peak and hole	+2.77 e$^-$/Å^3, − 1.68 e$^-$/Å^3	+5.10 and −3.96 e$^-$/Å^3
TWIN instruction	0 1 0 1 0 0 0 0−1 −4	0 1 0 1 0 0 0 0−1 −4
BASF parameters for TWIN	0.01(2), 0.50(2), 0.02(2)[a]	0.33(5), 0.18(4), 0.38(5)

[a]Note that significance of ESD of values 0.01(2) and 0.02(2) are with respect to values in the range of 0.00 to 1.00.

dra along the crystallographic c-axis. The fact that short face-sharing separations in NTO-like phases are not continuous, but instead, alternating with a wider separation of adjacent octahedra, allows for a wide variety of choices of cations for successful syntheses. However, when multiple types of cations are used, the appearance of "site mixing" often occurs and may be due to an overlap of at least one other component with an alternative structure.

In this study, we address the issue of whether the positions of different cations in apparent "mixed sites" are located at different positions or, as might be assumed in powder diffraction studies, are too close to each other to distinguish different positions about a single z-coordinate. Based on our single-crystal structure refinements, the small differences in positions of component cations for a given site are indeed significant. We report here, for the first time, the use of high-resolution X-ray data to determine precise parameters for composition, position, and ADP values of the atoms in the crystal structures of NTO-like phases Zn_2MnSbO_6 and Zn_2FeSbO_6.

2. EXPERIMENTAL SECTION

2.1. Synthesis. Polycrystalline samples with nominal composition Zn_2TSbO_6 (with T = Mn, Fe) were prepared under HPHT conditions starting from high-purity commercial reagents ZnO (Aldrich, 99.9% purity), Fe_2O_3 (Alfa Aesar, puratronic, 99.998% metals basis), Mn_2O_3 (Aldrich, 99.999% purity metals basis), and Sb_2O_5 (Alfa Aesar, puratronic, 99.998% purity metals basis). The mixture prepared for the synthesis conformed to the following reactions for the two Fe and Mn compounds, respectively:

$$4ZnO + Fe_2O_3 + Sb_2O_5 \rightarrow 2Zn_2FeSbO_6$$

$$4ZnO + Mn_2O_3 + Sb_2O_5 \rightarrow 2Zn_2MnSbO_6$$
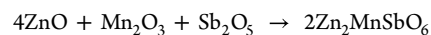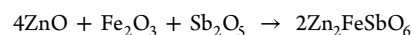
The reagents, weighed in a stoichiometric amount, were ground and homogenized in an agate mortar. The mixture was sealed in a Pt capsule and placed in an Al_2O_3 crucible. The so-prepared samples were loaded into a Walker-type multianvil press-apparatus[75,76] and pressurized to P = 7−8 GPa in 8−10 h. Once the final pressure was achieved, the samples were heated to 1250−1450 °C and the temperature was kept for 2−4 h. After the annealing time passed, they were quenched to temperatures of less than 150 °C on a time scale of 10 s by switching off the voltage supply of the resistance furnace.[75,76]

The pressure was maintained during both heating and quenching process, and only after completion of the cooling was the pressure slowly released over another 8−10 h.

2.2. Micrographic Analysis. Microstructure and morphology of the samples were checked by light optical microscopy (LOM) and scanning electron microscopy (SEM) (Leica Cambridge S360), in conjunction with energy-dispersive X-ray (EDS) spectroscopy (Oxford X-Max 20) for semiquantitative elemental analysis. The micrographic specimens were prepared by a standard polishing technique on representative sections of the samples. The EDS analyses were performed both on the overall area of the specimens and on single spots and small areas of small grains (0.5−1.0 μm^2). The accuracy of the measurements is within 2.0 atom % for O and 1.0 atom % for Zn, Fe, Mn, and Sb (within 1.0 atom % if O is not accounted for).

2.3. X-ray Diffraction Analysis. The crystal structures for the two compounds were investigated by SCD and PXRD. Small fragments (edge <50 μm) from the HPHT syntheses of Zn_2FeSbO_6 (sample TT1375) and Zn_2MnSbO_6 (sample TT1478) were examined using finely collimated Mo Kα X-radiation (λ = 0.71073 Å) at room temperature using a Rigaku XtaLAB Synergy-S diffractometer system. Reflection data to 0.36 Å resolution (θ = 80°) were processed with the CrysAlisPro software.[77] The X-ray data were indicative of a single lattice, with less than 1% noncoincident domains, e.g., due to nonmerohedral twinning, or multiple intergrowth crystallites. Such multidomain samples are expected to form and are indeed observed in other, discarded samples after HTHP syntheses followed by annealing periods of a few hours or less. In this report, the term "domain" will be used with respect to partition of coincident reflection data, and the term "component" will be used with respect to partition of structural models. For Zn_2FeSbO_6 and Zn_2MnSbO_6, reduction of diffraction data by use of programs SAINT[78,79] (routine XPREP) and PLATON[80] (routine TwinRotMat) revealed the presence of merohedral (racemic) and reticular merohedral (obverse/reverse) twinning, which was refined in SHELXL[81] by use of the TWIN and BASF instructions. Values of TWIN and BASF are included with crystallographic information for Zn_2FeSbO_6 (TT1375) and Zn_2MnSbO_6 (TT1478) in Table 2. The structure solution program SHELXT,[81] least-squares program SHELXL,[81] and GUI program ShelXle[82] were used for structure determination and refinement. The PXRD patterns were collected in the 2θ range between 15 and 120° by an X'Pert Philips diffractometer for Zn_2MnSbO_6 (sample TT1478) and a Bruker D8 Advance diffractometer for Zn_2FeSbO_6 (sample BB1388), both employing Cu Kα radiation (λ = 1.54184 Å) and a step size of 0.02° (2θ). The structural refinements by Rietveld method were performed by using the FullProf software suite.[83] The Mercury[84] program was used to visualize the structural models and create all crystallographic figures. VESTA[85] and TIDY[86] programs were used for calculations of geometries of octahedra and to determine the standardized positions of the atoms, respectively, and BVCalc[87] was used for bond valence calculations. Calculated precession photographs[77] of the 0kl, h0l, and hk0 zones of reflection data collected for Zn_2FeSbO_6 and Zn_2MnSbO_6 up to 0.5 Å resolution are given in Figures S1a−c and Figures S2a−c, respectively.

Complete tables of atomic positions, displacement parameters, and coordination geometries for the crystal structures of Zn_2FeSbO_6 (sample TT1375) and Zn_2MnSbO_6 (sample TT1478) are found in the Supporting Information , and CIF files have been deposited at CCDC with deposition numbers 2373123 and 2373124, respectively.

2.4. X-ray Absorption Near-Edge Spectroscopy (XANES). XANES data on Zn_2MnSbO_6 and Zn_2FeSbO_6 were collected in both the transmission and fluorescence modes with simultaneous standards on the beamline 7-BM (QAS) using a Si(111) channel cut monochromator at Brookhaven National Laboratory's National Synchrotron Light Source (NSLS-II). The data for the standard compounds were collected on NSLS-II (6-BM/7-BM) and NSLS-I (X-19A/X-18B) beamlines. All of the spectra were fit to pre and post edge backgrounds and normalized to unity absorption edge step across the edge.[13,35,72,88−92]

2.5. Optical Second Harmonic Generation (SHG) Measurement. The SHG measurements were carried out in reflection geometry at room temperature on properly polished samples with a modified WITec alpha 300S confocal Raman microscope. A pulsed fundamental beam generated by a Ti:sapphire system (l = 800 nm, repetition rate of 80 MHz, chopped at 1 kHz) was focused on the sample with a microscope objective. The polarization of the fundamental beam was controlled by a half-wave plate, and the SHG signal was detected with a photomultiplier tube after being passed through a polarization analyzer.

2.6. Physical Property Measurements. Magnetization measurements were performed with a physical property measurement system (PPMS, Quantum Design). The DC magnetization was measured in the temperature range 5−300 K for Zn_2FeSbO_6 and in the range 6−300 K for Zn_2MnSbO_6, under applied magnetic fields, H, of 1 kOe for the former and 1 kOe and 10 kOe for the latter. The isothermal magnetization, $M(H)$, was measured in applied fields up to ±70 kOe and at several temperatures. Zero-field heat capacity was measured between 2 and 100 K for Zn_2FeSbO_6 and between 2 and 150 K for Zn_2MnSbO_6.

3. RESULTS AND DISCUSSION

3.1. Phase Formation of Zn_2FeSbO_6 and Zn_2MnSbO_6. The PCD Zn_2FeSbO_6 (sample TT1375) and Zn_2MnSbO_6 (sample TT1478) were both prepared under P = 7 GPa, at T = 1350 °C; the former was heat-treated at 1350 °C for 2.5 h, while the latter was heat-treated for 4 h. Both samples were nearly single phase and containing large crystal grains of the target phase. Their microstructure was analyzed by both light optical microscopy (LOM) and scanning electron microscopy (SEM). The optical microscopy images are shown in Figure S3a,b and Figures S4a,d for Zn_2FeSbO_6 and Zn_2MnSbO_6, respectively. Both samples appear clean and containing mostly one phase of large and clean grains with size of ≈100 μm; they are transparent and deeply colored and gem-like. Polarized light accentuates the reflective anisotropy and transparent internal reflections (reddish areas in Figures S3b and S4d) in both compounds. No twinning was recognized in the reflected light optics.

The SEM microphotographs using both backscattered electron (BSE) and secondary electron (SE) modes for the two samples are shown in Figures S5a−c and S6a−c, respectively. For Zn_2FeSbO_6, the global analysis (carried out on the whole specimen area) is in very good agreement with the nominal starting composition "Zn_2FeSbO_6", with and without taking into account the oxygen content. An oxygen concentration of 57−59 at % (slightly lower than 60 at %) is acceptable given that O is a light element (and for it, only semiquantitative analysis can be performed); the sample is a quaternary compound; and our EDS-microprobe has an instrumental accuracy not better than about 2 at %. The Zn_2FeSbO_6 sample appears to be single phase (Figure S5b, BSE-mode); the darker areas are related to holes, fractures, and hollows of the sample surface (better evident in SE mode shown in Figure S5c). The point and small area EDS analyses carried out on some grains (Figure S5b) reveal the calculated composition to be close to $Zn_{20}Fe_{10}Sb_{10}O_{60}$ or $Zn_{50}Fe_{25}Sn_{25}$ if oxygen is not accounted for (with a likely accuracy of ±2 at %). No other extra phases appeared to be present in this sample. The same considerations apply for the Zn_2MnSbO_6 sample for which two specimens from sample TT1478 were analyzed. The global analysis for TT1478 measured with and without taking into account the oxygen content is in very good agreement with the nominal composition of "Zn_2MnSbO_6" (within the limit of about ±2 at %) (Figure S6a). The sample

is almost single-phase Zn_2MnSbO_6 (Figure S6c); a small amount of a pseudoternary phase with composition based upon EDS analysis of approximately $(Zn_{0.8}Mn_{0.3})Sb_2O_6$ was detected as small, elongated light-gray grains. The presence of this phase was confirmed by PXRD analysis and identified as ordonezite-type $ZnSb_2O_6$. For this TT1478 sample, the microphotograph image viewed in SE mode (Figure S6c) shows many gray grains pertaining to the target phase and dark areas pertaining to holes, fractures, or hollows. No further extra phases were observed optically in the TT1478 sample.

3.2. Crystal Structure of Zn_2FeSbO_6 and Zn_2MnSbO_6.

3.2.1. Single-Crystal X-ray Diffraction. Crystallographic information for the SCD experiments of Zn_2FeSbO_6 (sample TT1375) and Zn_2MnSbO_6 (sample TT1478) are given in Table 2. The unexpected unit volume difference at room temperature for these two compounds, namely, 320.38 Å^3 for the relatively heavier Zn_2FeSbO_6 and 327.42 Å^3 for relatively lighter Zn_2MnSbO_6, gives a first indication that differences in the two crystal structures were likely to be found. The space groups $R3c$ and $R\text{-}3c$ were immediately rejected since over 8% of all observed unique reflections (over 150) were in violation of the systematic absence rule for c-glide. By use of the entire, unaveraged sets of reflection data to a resolution limit of 0.38 Å ($\theta_{max} = 69.25°$) and programs XPREP[78,79] and PLATON,[80] it was determined that all apparently single-crystal samples examined contained merohedral twinning and belonged to the noncentrosymmetric space group $R3$. Structure solution by use of program SHELXT[81] for both data sets also selected the $R3$ model and indicated significant racemic twinning. Nevertheless, accurate sites for the Sb cation and the two O anions were easily found as well as approximate locations of the remaining cations. Determination of final occupancies per cation site was not straightforward, and not only the occupancies but also the cation coordination geometries and especially the residual electron densities were used to verify the model that best agreed with the reflection data. For the initial structural refinement of either sample, a check of the M-O bond distances and angles easily determined which site contained all or mostly Sb since that site gave six Sb-O bond distances close to the expected 1.98 Å value.[93] The Sb cation and both O anions were temporarily assigned full occupancy at this initial stage, which generally helped to determine any "mixing" of cations in all other sites based upon electron density and coordination geometry. These "mixed sites" were modeled by different two-component models for the Zn_2FeSbO_6 versus Zn_2MnSbO_6 crystals used here, as described in the following two sections. The crystal structural results obtained from different crystals selected from the synthetic batch of sample TT1375 (Zn_2FeSbO_6) were essentially identical, as were different crystals from sample TT1478 (Zn_2MnSbO_6).

3.2.2. Crystal Structure Determination of Zn_2FeSbO_6. The unit cell contents of the single-crystal sample of Zn_2FeSbO_6 (TT1375), which were determined by the program SHELXT, were translated in z to place the Sb cation at the (0 0 0) position. The Sb^{5+} cation site was the easiest to recognize because of its higher electron density and shortest M-O bonds. Positions and ADP for all atoms and site occupancies for the three remaining cations, initially considered as partially Zn, were then refined. The fractional z-coordinate for these three remaining cation sites refined at this initial point to $z = 0.712$, 0.496, and 0.217, and their occupancies converged to 92, 85, and 99% Zn, respectively. Next, but not finally, these cations

were refined as Zn(1), Fe(2), and Zn(3) to give occupancies 0.92, 1.07, and 0.99, thus confirming the sites to be mostly Zn, mostly Fe, and all Zn, respectively. Next, and also not finally, the placement of some Fe at the Zn(1) site and some Zn at the Fe(2) site followed by refinement of ADP for all ions gave the initial "single site" model listed in Table S1. These coordinates were also used for the initial model of the Rietveld refinement (*vide infra*). Thus, the sequential arrangement of cations along the c-axis is mostly Zn-Fe-Zn-Sb (NTO type) in coexistence with a lesser amount of Fe-Zn-Zn-Sb (OIL type) and generally agrees with so-called "mixed sites" models for M1 and M2 in the scheme M1-M2-M3-M4 (see Figure 1) modeled from
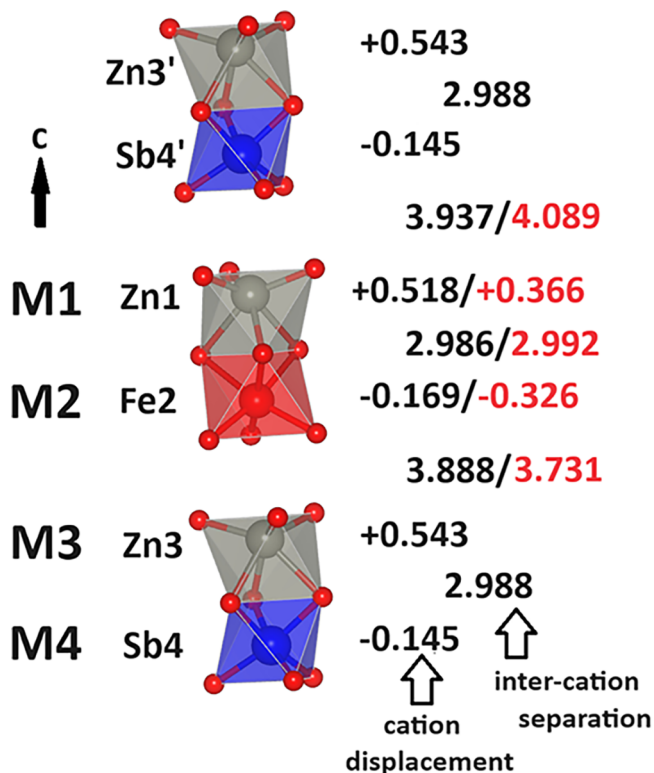

Figure 1. Displacements from centroids of octahedra and separations between adjacent cations along the c-axis for all cations in the crystal structure of Zn_2FeSbO_6 (TT1375); values for the main (68%) component are in black and for the second (32%) component are in red. The view is approximately along the [1−1 0 0] direction (e.g., crystallographic a-b diagonal). Polyhedral shading: Fe in red, Sb in blue, Zn in gray. Bond distances and angles for TT1375 are in Table S3; intercation distances are in Table S4.

several PXRD studies with M4 = Sb,[50] Mo,[68] Nb or Ta,[60] but apparently not Te. Examples of motifs with apparent mixing of M2 only[51] and of no mixing[30,50] do exist, as do examples of apparent mixing of both M1 and M3 with M4 = Sb[20] or M4 = Te[53] and of mixing of both M2 and M3 with M4 = Sb[18] or M4 = Te.[57]

Based upon the initial-stage ADP values for Zn(1) and Fe(2) in Table S1, it was observed that the U_{33} values were 3 and 2 times larger than the corresponding U_{11} values, respectively. As a result, a spatial separation between Zn and Fe atoms at the $z = 0.712$ and 0.496 sites was allowed to refine. A refinement with restrained and isotropic U and unrestrained z values for Zn(1) and Fe(1B) of site M1 gave z values of 0.713 and 0.708, respectively, and for Fe(2), and Zn(2B) of

Table 3. Finalized Refined Atomic Coordinates and Equivalent Isotropic Displacement Parameters, U_{eq}, for Zn_2FeSbO_6[a]

		atomic coordinates				
atom	Wyckoff site	x/a	y/b	z/c	occupancy	$U_{eq}[\text{Å}^2]$
Zn(1)	3a	0	0	0.7147(2)	0.678(8)	0.0091(3)
Fe(2)	3a	0	0	0.4983(3)	0.678(8)	0.0045(2)
Fe(1B)	3a	0	0	0.7037(5)	0.322(8)	0.0073(3)
Zn(2B)	3a	0	0	0.4870(4)	0.322(8)	0.0050(5)
Zn(3)	3a	0	0	0.21655(3)	1.0	0.0091(1)
Sb(4)	3a	0	0	0	1.0	0.00421(2)
O(1)	9b	0.0119(3)	0.3729(3)	0.2617(1)	1.0	0.0071(1)
O(2)	9b	0.2907(3)	0.3082(3)	0.0927(1)	1.0	0.0078(2)

[a] U_{eq} is defined as one third of the trace of the orthogonalized U_{ij} tensor. The minor component cations are designated by labels containing "B".

site M2 gave z values of 0.498 and 0.487, respectively. The Zn atoms at approximate site (0 0 0.71), Zn(1), and at approximate site (0 0 0.22), Zn(3), exhibited significant distortion from octahedral symmetry, as consistent with having the larger cation Zn^{2+} (0.74 Å[93]) at those sites. Final refinement gave 68% Zn at $z = 0.7146$, 32% Fe at $z = 0.7038$, 68% Fe at $z = 0.4982$, and 32% Zn at $z = 0.4869$, respectively. The final atomic coordinates and equivalent isotropic displacement parameters for Zn_2FeSbO_6 (TT1375) are given in Table 3, while the anisotropic thermal displacement parameters are collected in Table S2. This result is reproducible and independent of the starting positions and atom type for each partially occupied site, thus indicating a robust electron density basis for the derived result. Selected M-O bond distances and angles for Zn_2FeSbO_6 (TT1375) are given in Table S3, and the closest M-M intercation distances are in Table S4. A simple representation of the distortions from symmetrical octahedral distortion in TT1375, as shown in Figure 1, uses the displacement of each cation M from the centroid of its MO_6 octahedron. The centroid can simply be determined by the midpoint along the c-axis between the O1–O1–O1 and the O2–O2–O2 planes that are on either side of the cation. It is important to note that the minor components for the M1 and M2 sites, namely, Fe(1B) and Zn(2B), have coordination geometries in-between Zn(1) and Fe(2) and toward the direction of the observed geometry for Fe(2) and Zn(1). Thus, the minor component coordination geometries of Fe(1B) and Zn(2B) may represent transitional or hybrid geometries. Calculated bond valence sums[87] for $Zn(1)^{2+}$, $Fe(2)^{3+}$, $Zn(3)^{2+}$, $Sb(4)^{5+}$, $Fe(1B)^{3+}$, and $Zn(2B)^{2+}$ are +2.01, +2.74, +1.93, +4.96, +2.35, and +2.38, respectively. Also shown in Figure 1 are the separations between adjacent cations along the c-axis. A depiction of the nearest-neighbor octahedra about the four cation sites in Zn_2FeSbO_6 (TT1375) is given in Figure 2, and the coordination geometries of individual cations are depicted in Figure S7. Thus, for the crystal structure of Zn_2FeSbO_6 (TT1375), a cocrystal model with common Zn(3) and Sb(4) sites and Zn and Fe cations, respectively, in the M1 and M2 sites (the major component case) and Fe and Zn cations, respectively, in the M1 and M2 sites (the minor component case) is obtained. In terms of standard phase types, the major Zn-Fe-Zn-Sb component is NTO, and the minor Fe-Zn-Zn-Sb component is OIL. Thus, for the crystal structure of Zn_2FeSbO_6 (TT1375), the cation located in the so-called "anti-site" of (0 0 0.50) with respect to the Sb cation at (0 0 0) is not restricted to Fe^{3+} alone. As a result, the physical properties of Zn_2FeSbO_6 may be hybridized between those of the NTO phase and those of the OIL phase. This model of NTO/OIL cocrystal was observed in four compounds from
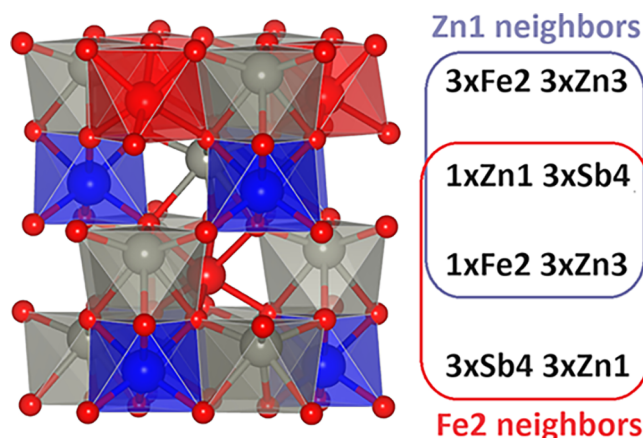

Figure 2. Diagram of nearest-neighbor octahedra to the Zn(1) cation (gray, unshaded) and Fe(2) cation (red unshaded) for the main (68%) component of the crystal structure of Zn_2FeSbO_6 (TT1375); (shaded polyhedra for Fe in red, Zn in gray, and Sb in blue). Nearest-neighbor distances in TT1375 are in Table S4.

three previous powder diffraction studies noted above,[25,33,40] but not in any previous SCD study to date.

3.2.3. Crystal Structure Determination of Zn_2MnSbO_6. For the single-crystal sample of Zn_2MnSbO_6 (TT1478), the above procedure for structure determination was followed up to the point of finding an initial M1-M2-Zn(3)-Sb(4) structural solution. However, for the next step, namely, the selection of cation types for mixed or unmixed M1 and M2 sites, the previously Zn_2FeSbO_6 cocrystal model of superimposed NTO and OIL components failed. Instead, the best structural model for Zn_2MnSbO_6 (TT1478) was found to be that of a cocrystal of two nearly identical OIL-like phases, namely, about 80% Mn-Zn-Zn-Sb superimposed with about 20% Sb-Zn-Zn-Mn. These two OIL phases are NOT related by crystallographic symmetry, nor by any twinning operation. From PXRD results of previous studies, 100% occupancy of the B′ cation at the M4 site is common and perhaps assumed for successful Rietveld analysis such that previous evidence of a slightly mixed M4 site is expected to be rare and has been reported for only one compound.[30]

Based upon electron densities, M1 and M4 sites were found to be split, mixed with a ratio 84:16 and complementary. Namely, refinement converged at 84% for Mn(1) at $z = 0.6999$ and 84% for Sb(4) at $z = 0.0$ (fixed as origin) and 16% for Sb(1B) at $z = 0.6858$ and 16% for Mn(4B) at $z = -0.0144$, respectively (Table 4). The electron densities at sites M2 and M3 were found to be consistent with Zn only and also split. Namely, for site M2, $z = 0.4919$ for Zn(2) and 0.4726 for

Table 4. Finalized Refined Atomic Coordinates and Equivalent Isotropic Displacement Parameters, U_{eq}, for Zn_2MnSbO_6[a]

| atom | Wyckoff site | atomic coordinates | | | occupancy | $U_{eq}[Å^2]$ |
		x/a	y/b	z/c		
Mn(1)	3a	0	0	0.6999(2)	0.842(5)	0.0161(4)
Zn(2)	3a	0	0	0.4921(2)	0.842(5)	0.0090(3)
Zn(3)	3a	0	0	0.2129(1)	0.842(5)	0.0125(1)
Sb(4)	3a	0	0	0	0.842(5)	0.0071(1)
Sb(1B)	3a	0	0	0.6858(2)	0.158(5)	0.0059(3)
Zn(2B)	3a	0	0	0.4730(3)	0.158(5)	0.0090(3)
Zn(3B)	3a	0	0	0.1836(4)	0.158(5)	0.0125(1)
Mn(4B)	3a	0	0	−0.0142(5)	0.158(5)	0.0071(1)
O(1)	9b	0.0121(6)	0.3699(8)	0.2626(2)	1	0.0126(3)
O(2)	9b	0.3015(9)	0.2994(8)	0.0893(2)	1	0.0151(4)

[a]U_{eq} is defined as one third of the trace of the orthogonalized U_{ij} tensor. The minor component cations are designated by labels containing "B".

Zn(2B), and for site M3, $z = 0.2130$ for Zn(3) and 0.1835 for Zn(3B). The cation occupancies and splitting for Zn_2MnSbO_6 (TT1478) are depicted in Figure 3. Although the occupancies
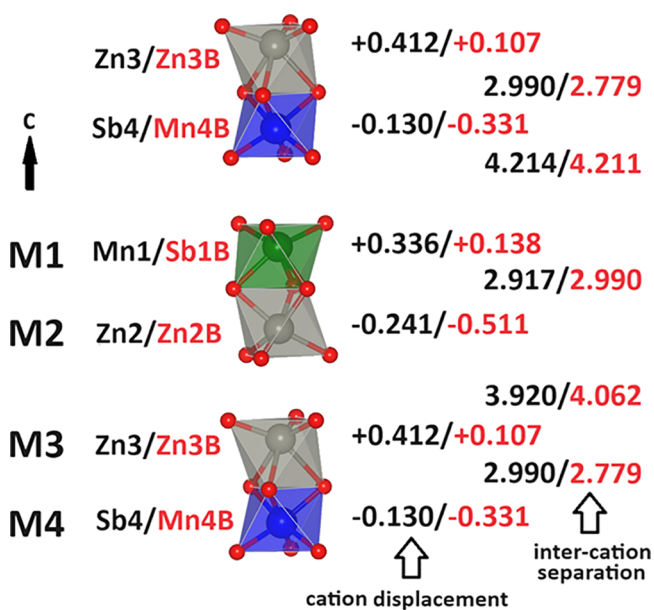
Figure 3. Displacements from centroids of octahedra and separations between adjacent cations along the *c*-axis for all cations in the crystal structure of Zn_2MnSbO_6 (TT1478); values for the major (84%) component are in black and for the minor (16%) component are in red. The view is approximately along the $[1{-}1\ 0\ 0]$ direction (e.g., crystallographic *a*-*b* diagonal). Polyhedral shading: Mn in green, Sb in blue, Zn in gray. Bond distances and angles for TT1478 are in Table S6; intercation distances are in Table S7.

of Zn(3) and Zn(3B) refined to a similar ratio (0.86:0.14) to those found for sites M1 and M4 (0.84:0.16), the occupancies of Zn(2) and Zn(2B) for site M2 refined to 0.66 and 0.24, respectively. Thus, it appears that the site splitting for M3 is correlated to that of its face-shared partner M4, but the site splitting for M2 is independent of that of its face-shared partner M1. Refinements using either Mn or Sb for the M2 or M3 site did not yield a significantly different result than the all-Zn model and were not consistent with the stoichiometry from EDS measurements. Since the site M2 is near $z = 0.5$ and has a significantly different mixing than the three other sites, the possibility of a commensurate modulation of period $c/2$ (or,

$2c*$) for the site occupancies exists, and models of such a structural modulation are being explored.

For the crystal structure of Zn_2MnSbO_6 (TT1478), anisotropic displacement parameters are collected in Table S5, the M-O bond distances and angles for all atoms are given in Table S6, and M-M intercation distances are in Table S7. Calculated bond valence sums[87] for Mn(1)$^{3+}$, Zn(2)$^{2+}$, Zn(3)$^{2+}$, Sb(4)$^{5+}$, Sb(1B)$^{5+}$, Zn(2B)$^{2+}$, Zn(3B)$^{2+}$, and Mn-(4B)$^{3+}$ are +2.66, +1.96, +1.85, +4.95, +4.24, +2.01, +2.00, and +3.26, respectively. Cation coordination geometries for Zn_2MnSbO_6 (TT1478) are shown in Figure S8. The major and minor components of the crystal structure of Zn_2MnSbO_6 are depicted in Figure 3 and are not related by crystallographic symmetry but rather by a 2-fold axis nearly parallel to the $[1{-}1\ 0\ 0]$ direction of the reticular merohedry axis already taken into account by use of TWIN and BASF instructions (SHELXL). Thus, the two components of Zn_2MnSbO_6 (TT1478) are neither related by additional twinning, nor any $R3$ symmetry operation, nor by inversion. Instead, the noncrystallographic 2-fold symmetry maintains two unequal polar components of approximate ratio 80:20 and having the same two unique and well-defined O anion positions that, in combination, maintain a smaller, but nonzero, net polarity overall (e.g., based upon BASF parameters on the order of 0.2; see Table 2). Nearest-neighbor octahedra about the four cation sites in Zn_2MnSbO_6 (TT1478) are shown in Figure 4. It is noted here that the structures of both components of Zn_2MnSbO_6 (TT1478) are isomorphs with the minor component in the model of Zn_2FeSbO_6 (TT1375), which is the OIL type. This difference in cocrystal model between Zn_2FeSbO_6 and Zn_2MnSbO_6 may explain the unusual relationship between their unit cell volume and formula weight and perhaps also between their differing physical properties, especially frustration of magnetization (*vide infra*). In other words, physical property differences may be due to different motifs of alternating cations along the *c*-axis for the NTO versus the OIL motifs (see Figures 1 and 3).

3.2.4. Rietveld Refinement of Zn_2FeSbO_6 and Zn_2MnSbO_6. The structure was further confirmed by Rietveld refinement on the powder data for both compounds. Two representative X-ray powder patterns including the Rietveld fit for the two compounds are shown in Figure S9a,b for Zn_2FeSbO_6 (sample GG1388) and Zn_2MnSbO_6 (TT1478). The atomic coordinates and isothermal parameters, B_{iso}, obtained from Rietveld refinement for the two compounds are collected in Tables S8 and S9. For Zn_2FeSbO_6, the final refined occupancy factor for Zn/Fe in the Wyckoff site 3a (0 0 0.5052) and the Fe/Zn ratio

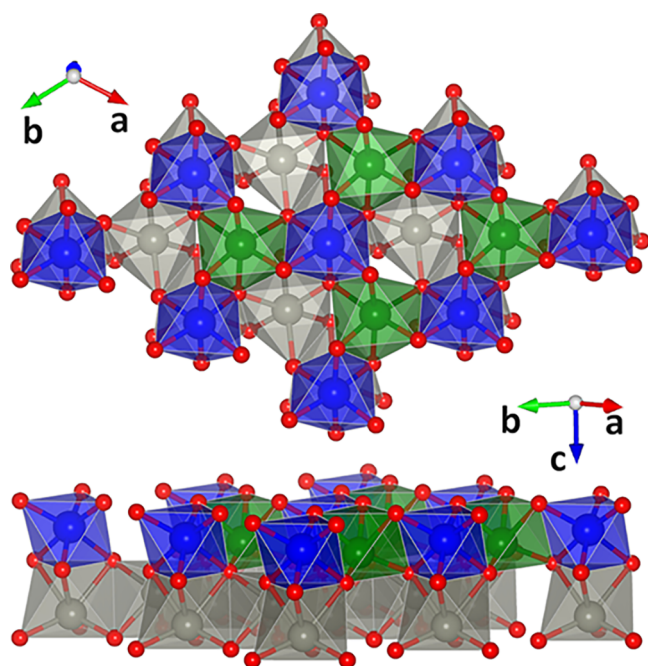**Figure 4.** Projections of the packing of face-sharing octahedra in the crystal structure of Zn_2MnSbO_6 (TT1478); the views are approximately along the crystallographic c-axis (top panel) and (a +b) diagonal axis (bottom panel). The ordered ilmenite structure of Zn_2MnSbO_6 (TT1478) is characterized by longer Mn^{3+} to Sb^{5+} distances *via* their edge-sharing octahedra in the a-b plane than the Mn^{3+} to Zn^{2+} distances *via* face-sharing octahedra along the a-b plane normal direction (c-axis). These distances are tabulated in Table S7. In the crystal structure of Zn_2MnSbO_6, unlike Zn_2FeSbO_6, there is only face sharing to Zn^{2+} octahedra (Mn in green, Sb in blue, Zn in gray).

in the 3a (0 0 0.7131) sites were almost the same for both Rietveld and single-crystal analyses: 0.716(6):0.284(6) (Rietveld) vs 0.678(8)):0.322(8) (single crystal). For Zn_2MnSbO_6, the refinement was performed by using the average values of the coordinates obtained from averaging the values of the two OIL components from single-crystal analysis; the resulting Mn/Sb ratio in the 3a (0 0 0) and 3a (0 0 0.6905) sites is 0.819(2):0.181(2) (Rietveld) vs 0.792(4):0.208(4) (single crystal). Both refinements corroborate the Zn_2FeSbO_6 (sample GG-1388) and Zn_2MnSbO_6 (sample TT1478) stoichiometry.

While the Zn_2FeSbO_6 bulk sample is a single phase (or extra phases are not detectable by PXRD), two impurities are detected in the Zn_2MnSbO_6 bulk sample. One impurity is the $Zn_{1-x}Mn_xSb_2O_6$ (ordonezite), with $x \approx 0.3$, as determined by SEM-EDS, adopting the anti-Ta_2FeO_6-type structure ($tP18$, $P4_2/mnm$, no. 136), and the other is $LaCrO_3$ ($SrTiO_3$-type phase, $cP5$, Pm-$3m$, no. 221), likely a residual contaminant derived from the heater used during the HTHP synthesis and mixed into the sample on retrieval from the HPHT assembly.

3.2.5. Discussion of Single-Crystal Structure Results. The relative tilts of octahedra are determined solely by the O anion positions, and these positions are the least well-known when using PXRD data. Use of neutron powder diffraction (NPD) may give more reliable O anion positions but generally requires large quantities of sample so that high-resolution single-crystal data, even from in-house X-ray diffractometers, may offer an excellent alternative in seeking accurate O anion positions. We have found, in agreement with other researchers' results or assumptions, that the relative octahedral tilts determined by the positions of the O anion vary only slightly from one compound to another, regardless of type, NTO or OIL.

For all MO6 octahedra in samples Zn_2FeSbO_6 (TT1375) or Zn_2MnSbO_6 (TT1478) used in this study, the SbO_6 octahedra were the most regular, if not nearly m-symmetrical (Table 5). Based upon the distortion index,[85] octahedra with minor distortion were found for the Fe^{3+} in the dominant (68%) component of Zn_2FeSbO_6 and for the Sb^{5+} sites of either component of Zn_2MnSbO_6 (see Table 5). The most distorted octahedra are those of sites containing the Zn^{2+} cation in any of the Zn sites of any component of either Zn_2FeSbO_6 or Zn_2MnSbO_6. The consequences of severe distortions from octahedral geometry for the larger Zn^{2+} cation versus Fe^{3+} or Mn^{3+}[93] have been mentioned in previous reports[1,15,72] and is quantified in this study by the cation offsets from the approximate centers of their respective octahedra shown in Figures 1 and 3.

For either of the title compounds, the two largest distortions occur at sites of the two largest octahedral volumes. Also, it appears that the octahedra with volumes of less than 10.4 Å³ may prefer Sb^{5+} with little or no mixing and the octahedra with volumes of more than 12.0 Å³ may prefer Zn^{2+} and no mixing (Table 5). The computed octahedral volumes show important irregularities, especially for the octahedra of mixed cation sites M2 in Zn_2FeSbO_6 and M1 in Zn_2MnSbO_6. For the M2 site in

Table 5. Geometric Details for the Four Unique Cation Octahedra in Zn_2FeSbO_6 (TT1375) and Zn_2MnSbO_6 (TT1478)[a]

Cation	z- coordinate	Average bond length [Å]	Site octahedral volume [Å³]		Distortion index [Å]	Quadratic elongation	Bond angle variance [deg²]
TT1375			(see **Figure 1**)				
Zn1/Fe1B	0.7147/0.7037	2.141/2.114	**M1**	11.86	0.073/0.037	1.073/1.042	218/135
Fe2/Zn2B	0.4983/0.4869	2.050/2.066	**M2**	11.35	0.015/0.058	1.009/1.027	30/83
Zn3	0.2166	2.154	**M3**	12.02	0.072	1.077	231
Sb4	0.0000	1.987	**M4**	10.35	0.013	1.007	25
TT1478			(see **Figure 3**)				
Mn1/Sb1B	0.6999/0.6858	2.074/2.054	**M1**	11.32	0.047/0.005	1.036/1.013	114/46
Zn2/Zn2B	0.4921/0.4729	2.121/2.160	**M2**	12.44	0.023/0.092	1.016/1.062	54/177
Zn3/Zn3B	0. 2129/0.1836	2.173/2.118	**M3**	12.52	0.074/0.034	1.067/1.009	202/27
Sb4/Mn4B	0.0000/-0.0143	1.987/2.006	**M4**	10.34	0.007/0.063	1.008/1.031	27/95

[a]All parameters are from program VESTA.[85] Cations ordered along the crystallographic c-axis shown in Figure 1 or Figure 3 as M1-M2-M3-M4 have fractional coordinates (0 0 z). The volumes of face-sharing octahedra are highlighted by red and blue shading.

Zn_2FeSbO_6, if not for the use of HP during synthesis, it may appear unusual that a Zn^{2+} cation would occupy a site with a volume as small as 11.35 Å^3. However, the average Zn−O bond length at that site is 2.066 Å and only 0.054 Å shorter than the expected 2.12 Å Zn−O bond length at ambient pressure[93] and the Zn(2B) octahedron at that site has moderate distortion as exhibited by its distortion index of 0.058 Å, which is less than those of Zn(1) and Zn(3) at the M1 and M3 sites of Zn_2FeSbO_6 with distortion indices of 0.074 and 0.071 Å, respectively. It is noted here that distortions of all octahedra in the crystal structures of Zn_2FeSbO_6 and Zn_2MnSbO_6 are prolate (elongation) rather than oblate (flattened), even though the anisotropic displacement parameters are either prolate or slightly oblate. The complementary site mixing for Zn_2FeSbO_6 in our model occurs between sites M1 and M2. The placement of Fe^{3+} at the M1 site is unexpected since the Fe^{3+} cation should prefer sharing with the higher valent Sb^{5+} site at M4 rather than the Zn^{2+} site at M1. However, that is not the case here and the average Fe−O bond length at the M1 site (2.112 Å) is 0.087 Å longer than the expected 2.025 Å bond length[93] and 0.062 Å longer than that observed for the Fe^{3+} in site M2 with its octahedra volume of 11.35 Å^3, which is comparatively intermediate in size. As noted above, for both M1 and M2 sites of Zn_2FeSbO_6, the minor Fe^{3+} and Zn^{2+} components, Fe(1B) and Zn(2B), respectively, each have an average bond length that is between expected Zn−O and Fe−O values.

For face-sharing octahedra in the crystal structure of Zn_2MnSbO_6, namely, M1/M2 and M3/M4, the octahedral distortions (Table 5) for Mn(1) and Zn(2) (which have a face-shared M1-M2 distance of 2.917(4) Å, as shown in Figure 3) are moderate (e.g., < 0.05 Å) and similar in magnitude. In contrast, the other face-shared octahedra in Zn_2MnSbO_6 (M3-M4, with an M3-M4 distance of 2.990(1) Å, as shown in Figure 3) show a large distortion for Zn(3) with a distortion index of 0.074 Å and small distortion for Sb(4) with a distortion index of 0.007 Å. For structure refinement of site M1, with the greater distortion of the Mn(1) octahedron (distortion index of 0.047 Å) versus distortion of the same-site Sb(1B) octahedron (distortion index of 0.005 Å), the corresponding ADP parameters were not constrained to be equal and refined to reasonable values based upon refined ADP values for Zn(2) and Sb(4) cations, respectively. This difference in distortions observed here for face-sharing pairs of octahedra may be related to the different modes of Zn cation splitting for sites M2 versus M3 (with or without any structural modulation) and intraface interaction energy calculations ought to shed light on this difference as well as the unexpected site mixing mode of face-sharing octahedra in Zn_2FeSbO_6.

Based upon effective ionic radius (ir),[93] we would expect Fe^{3+} (high-spin Fe^{3+} d^5, ir = 0.645 Å) and Mn^{3+} (high-spin Mn^{3+} d^4, ir = 0.645 Å) to mix with Sb^{5+} (ir = 0.6 Å), rather than with the larger Zn^{2+} (ir = 0.74 Å) in the crystal structures of Zn_2FeSbO_6 and Zn_2MnSbO_6. Hence, why Fe^{3+} mixes with Zn^{2+} and not with Sb^{5+} in Zn_2FeSbO_6 while Mn^{3+} mixes with Sb^{5+} in Zn_2MnSbO_6 and not with Zn^{2+} is likely not due to a size effect, but an electronic effect, due to differences of individual octahedral environments and interactions between neighboring octahedra for the different NTO and OIL motifs shown in Figures 1 and 3. With respect to intercation distances along the z-axis shown in those figures, the narrow range of face-shared M-M distances for both components of

Zn_2FeSbO_6, 2.98 to 2.99 Å, is nearly the same as the range for three of the four M-M distances in Zn_2MnSbO_6, 2.92 to 2.99 Å (Tables S4 and S6). However, the 2.78(1) Å M3-M4 distance in Zn_2MnSbO_6 involving the 16% Mn(4B) cation that shares its M4 site with 84% Sb(4) may not be as accurately determined because of the mismatch of smaller electron density due to 16% Mn ($4e^-$) versus that due to 84% Sb ($44e^-$). Such a mismatch in Z does not exist for any other mixed cation site in Zn_2FeSbO_6 or Zn_2MnSbO_6. The values of intercation distances for separations between the face-sharing octahedra (e.g., the rather open separations) are noticeably longer for the major component of Zn_2MnSbO_6, 3.92 to 4.21 Å, than for the major component of Zn_2FeSbO_6, 3.89 to 3.94 Å. These cation−cation separations are consistent with the larger unit cell volume for Zn_2MnSbO_6 compared to that for Zn_2FeSbO_6 (Table 2) and likely consistent with greater repulsive forces between face-sharing octahedra in the former compound than in the latter. Such differences in intercation forces for the two title compounds are the basis of their differences in "mixing" and of their physical property differences.

As shown in Figure 2, the 13 nearest-neighbor octahedra to M1 (with z ∼ 0.70) in Zn_2FeSbO_6 (and also in Zn_2MnSbO_6, since the octahedra are formed from O anions alone) are the one face-sharing M2 octahedron; three edge-sharing octahedra to M4 sites related by rhombohedral symmetry; six corner-sharing octahedra to M2 and M3 sites related by rhombohedral symmetry toward the +c direction; and three corner-sharing octahedra to M3 sites related by rhombohedral symmetry toward the -c direction. For significant adjacent site influence on distortions of the M1 site, the face-sharing site M2 should be the major contributor followed by the 3-fold related edge-sharing sites at M4' with symmetry 1/3, 2/3, z+2/3 for any NTO- or OIL-like phase. The complementary (or corresponding) mixing to site M1 for Zn_2FeSbO_6 is found in site M2 and to site M1 for Zn_2MnSbO_6 is found in site M4. Thus, for both compounds, complementary mixing to that found in site M1 appears to be less favored at site M3 (where only Zn^{2+} is found) due to less proximity. The situation for site M2 is not like that of site M1 but has relevance only for Zn_2FeSbO_6. For site M2, there is face-sharing to site M1 octahedra. Next closest sites to M2 are M3 sites with their edge-sharing octahedra, unmixed and only containing Zn^{2+} cations. Thus, with respect to site M2, there may be only one favorable complementary site for mixing, namely, that of the face-shared octahedron. This nonreciprocal relationship is consistent with polar compounds. Calculated cation−cation interaction energies and correlations for M1 and M2 pairings of site mixing, as in Zn_2FeSbO_6, versus M1 and M4 pairings as in Zn_2MnSbO_6, should help us understand why these compounds have different pairing motifs, and such calculations are the subject of our future research on these compounds.

3.3. Physical Properties of Zn_2MnSbO_6 and Zn_2FeSbO_6. The zero-field heat capacity was measured between 2 and 100 K for Zn_2FeSbO_6 and between 2 and 150 K for Zn_2MnSbO_6; the data are shown in Figure 5a,b. Both curves follow a similar trend and reveal a broad and weak hump around ≈9 K for Zn_2FeSbO_6 and at ≈5.5 K for Zn_2MnSbO_6. This anomaly may be consistent with low-temperature magnetic ordering and/or magnetic frustration

To investigate in more detail the magnetic properties for these two compounds, the temperature dependence of magnetic susceptibility, $\chi(T)$, was measured between 5 and
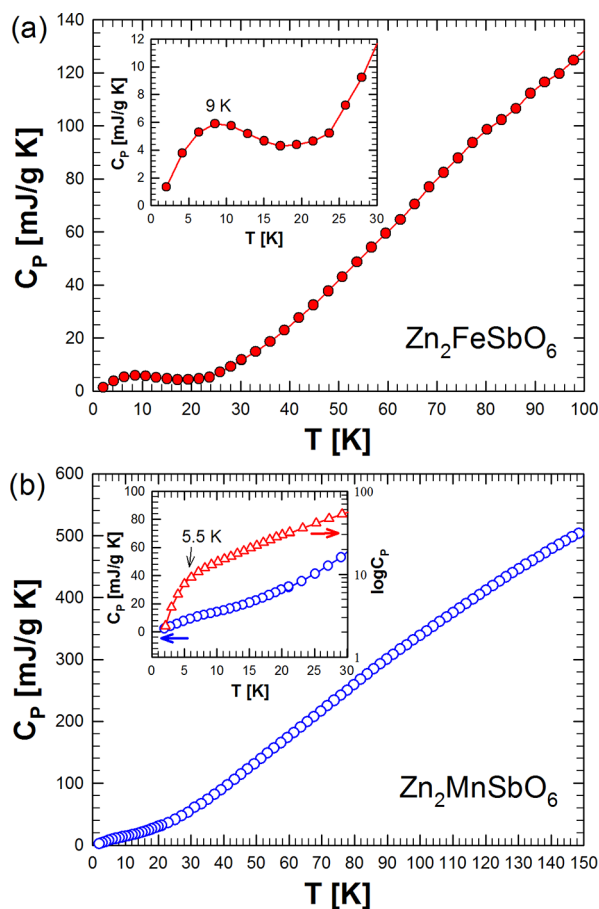
Figure 5. (a) Zero-field heat capacity, C_P, between 2 and 100 K for Zn_2FeSbO_6; the inset shows a magnification of the data in the range 2−30 K. (b) Zero-field heat capacity, C_P, between 2 and 150 K for Zn_2MnSbO_6; the inset shows a magnified view of the data in the range 2−30 K, displayed on both linear (blue circular symbols) and logarithmic scales (red triangular symbols) to better highlight the anomaly.

300 K and under applied magnetic field H = 1 kOe for Zn_2FeSbO_6 (Figure 6) and between 2 and 300 K and under
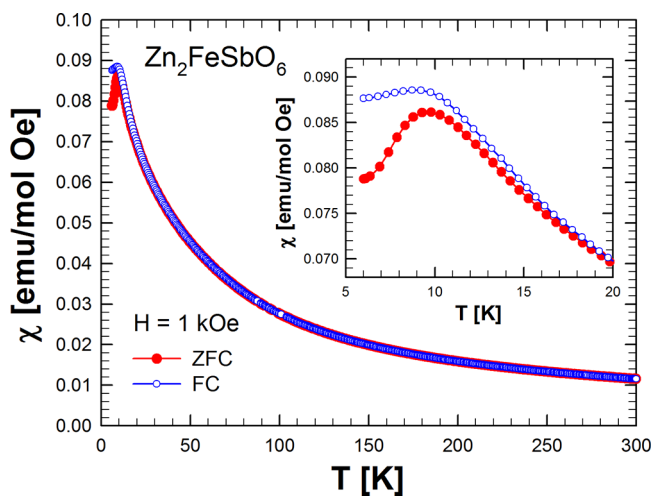
Figure 6. Magnetic susceptibility, $\chi(T)$, in the range 5−300 K and under applied magnetic field H = 1 kOe for Zn_2FeSbO_6; the inset shows a magnification of the data in the range 5−20 K.

applied magnetic fields H = 1 and 10 kOe for Zn_2MnSbO_6 (Figure 7a,b). The data were collected both in zero-field-
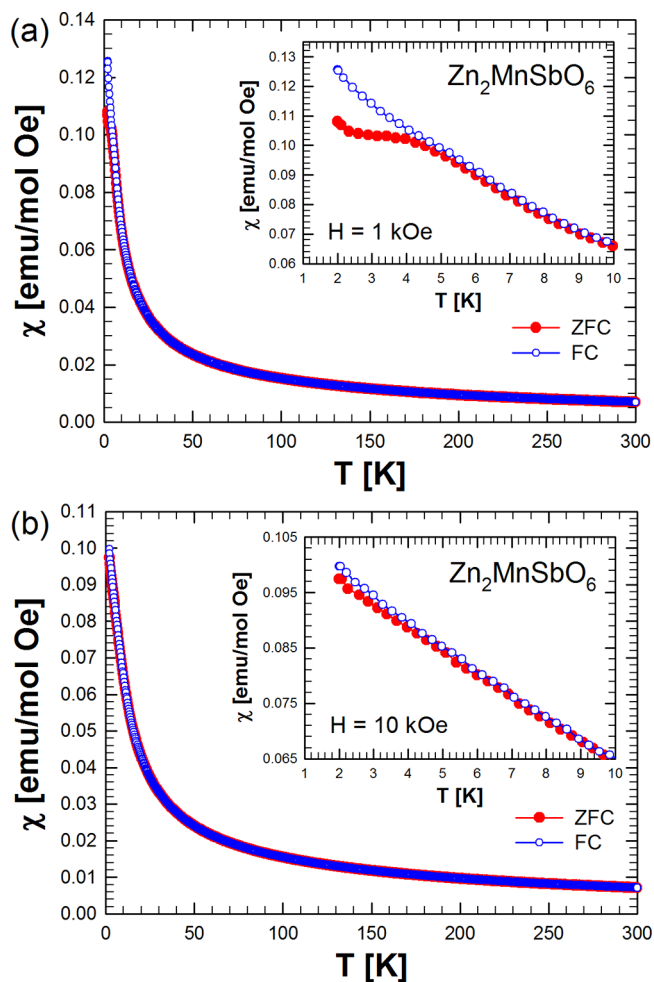
Figure 7. (a) Magnetic susceptibility, $\chi(T)$, in the range 2−300 K and under applied magnetic fields H = 1 kOe (a) and 10 kOe (b) for Zn_2MnSbO_6; the insets show a magnification of the data in the range 2−10 K.

cooled (ZFC) and field-cooled (FC) modes. The magnetic susceptibility for Zn_2FeSbO_6 reveals a distinct peak at ≈9 K, which is characteristic of an antiferromagnetic (AFM) transition. The Néel temperature, T_N, assuming that it corresponds to the peak temperature, is 9 K. Both ZFC and FC curves superimpose from room temperature down to around 20 K, after which thermomagnetic irreversibility emerges between the two data sets (inset of Figure 6). This phenomenon may be indicative of either magnetic anisotropy or the presence of spin-glass state in Zn_2FeSbO_6.[94,95] For Zn_2MnSbO_6, the ZFC data at H = 1 kOe reveal a small hump around 4 K, suggesting a possible spin-glass-like transition with antiferromagnetic interactions. This feature is absent in the FC data at H = 1 kOe and is suppressed under a higher field of 10 kOe. Similar to Zn_2FeSbO_6, the Zn_2MnSbO_6 compound also exhibits thermomagnetic hysteresis in both the ZFC and FC curves below approximately 10 K (inset of Figure 7a). The inverse magnetic susceptibility, $1/\chi(T)$, as a function of temperature for Zn_2FeSbO_6 and Zn_2MnSbO_6 is plotted in Figure S10a,b. The data vary linearly as a function of temperature in the paramagnetic region, i.e., between 200

and 300 K. The least-squares fit to the Curie–Weiss law [$\chi(T)$ = $C/(T - \theta_{CW})$, where C is the Curie constant and θ_{CW} is the Curie–Weiss temperature] between this temperature range gives values of $\theta_{CW} = -60$ K for Zn_2FeSbO_6 and $\theta_{CW} = -79$ K for Zn_2MnSbO_6. The negative value of the Curie–Weiss temperature corroborates the AFM ground state for Zn_2FeSbO_6 and the presence of AFM exchange interactions between the spins in Zn_2MnSbO_6. The effective magnetic moment, μ_{eff}, obtained from the Curie–Weiss fit is 5.76 μ_B/f.u. for Zn_2FeSbO_6 and 4.58 μ_B/f.u. (at $H = 1$ kOe) and 4.64 μ_B/f.u. (at $H = 10$ kOe) for Zn_2MnSbO_6. If we consider that the theoretical value of magnetic moment for Fe^{3+}, assuming the high-spin-only contribution ($3d^5$, $^6S_{5/2}$), is 5.92 μ_B,[96] our experimental value is consistent with the presence of high-spin Fe^{3+} cations in Zn_2FeSbO_6. This is in agreement with the XANES data (see Section 3.3). The calculated magnetic moment for Mn^{3+} assuming high-spin-only contribution ($3d^4$, S = 2), is 4.91 μ_B, while the value for Mn^{2+}, assuming high-spin-only contribution ($3d^5$, S = 5/2), is 5.92 μ_B. The effective magnetic moment observed in Zn_2MnSbO_6, 4.58–4.65 μ_B, is in agreement with the expected value for Mn^{3+} cations, in agreement with the XANES data (see Section 3.3). The fact that the values are slightly lower than the expected value may be due to crystallographic disorder.

For both compounds, the frustration parameter, f, was calculated to shed more light on the possible magnetic frustration of these two materials. The frustration parameter is defined by the absolute value of the ratio between the Curie–Weiss temperature and the temperature at which the magnetic order "freezes",[97] i.e., $f = |\theta_{CW}|/T_N$. For Zn_2FeSbO_6, $\theta_{CW} = -60$ K and $T_N = 9$ K, so $f = 6.7$, while for Zn_2MnSbO_6, $\theta_{CW} = -79$ K and $T_N = 4$ K, so $f = 19.8$. These values indicate moderate magnetic frustration in Zn_2FeSbO_6 and more significant magnetic frustration in Zn_2MnSbO_6. It has been observed that values for $f > 5-10$ indicate a strong suppression of magnetic ordering as a result of frustration, which is likely the case of Zn_2MnSbO_6. Moreover, for such high f values, the temperature range $T_N < T < |\theta_{CW}|$ defines the spin-liquid regime.[97] Therefore, if we consider that our f values are ≈7 and ≈20, respectively, for the two compounds, we can determine that the spin-liquid regime is in the range 9–60 K for the Fe compound and in the range 4–79 K for the Mn compound. The higher magnetic frustration observed in Zn_2MnSbO_6 compared to Zn_2FeSbO_6 could be due to the higher % of the OIL-type phase present in the former compound. Specifically, 100% of the nonface-shared octahedra in the Mn compound have c-axis nearest-neighbor Zn–Zn and Sb–T distances of 4 Å, whereas only 32% of the face-shared octahedra in the Fe compound exhibit these Zn–Zn and Sb–T distances (compare Figures 1 and 3). Additionally, the Fe^{3+} cation is more polarizable than Mn^{3+}, as it has one more unpaired electron compared to that of Mn^{3+}. This higher polarizability facilitates stronger AFM interactions in Zn_2FeSbO_6, contributing to more stable magnetic ordering. In contrast, the lower polarizability of Zn_2MnSbO_6 plays a role in the enhanced magnetic frustration observed, where competing interactions and potential disorder prevent the system from achieving a fully ordered magnetic state.

The isothermal magnetization vs applied magnetic field, $M(H)$, measured at various temperatures ($T = 5, 10, 20, 30, 40, 50,$ and 300 K for Zn_2FeSbO_6 and $T = 2, 5, 150,$ and 300 K for Zn_2MnSbO_6) is presented in Figure 8a,b for Zn_2FeSbO_6 and Zn_2MnSbO_6. At $T = 300$ K, both compounds are in the

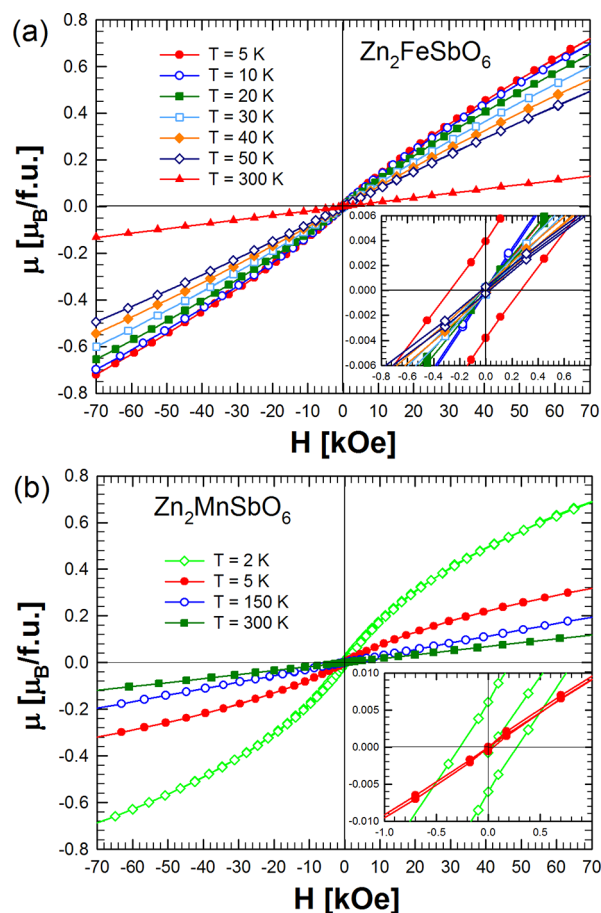**Figure 8.** Isothermal magnetization of Zn_2FeSbO_6 at $T = 5, 10, 20, 30, 40, 50,$ and 300 K (a) and Zn_2MnSbO_6 at $T = 2, 5, 150,$ and 300 K (b), measured up to $H = \pm 70$ kOe. The insets show magnified views of the data in the range ± 0.8 kOe for Zn_2FeSbO_6 and ± 1.0 kOe for Zn_2MnSbO_6 at temperatures within the spin-liquid region.

paramagnetic state, as is clearly shown by the $M(H)$ curves collected at room temperature. For the Mn compound, the paramagnetic behavior persists at $T = 150$ K (Figure 8b). The curves measured between 50 and 2 K for Zn_2FeSbO_6 and at 5 and 2 K for Zn_2MnSbO_6 display a broad "S" shape with no sign of saturation at high applied magnetic fields. This trend is typical of spin-glass behavior, characterized by a nonlinear increase in magnetization as the applied magnetic field increases, indicating disordered and frustrated spin interactions. It also provides clear evidence of competing antiferromagnetic (AFM) interactions underlying the magnetic frustration in both compounds. For both compounds, the magnetization initially rises slowly at low fields followed by a more rapid increase at higher fields, without saturating due to competing interactions between spins, which prevent them from aligning even under high magnetic fields. This feature is more pronounced for Zn_2MnSbO_6 than for Zn_2FeSbO_6. In Zn_2MnSbO_6, the deviation from the linear paramagnetic trend is clearly evident at $T = 5$ K, whereas for Zn_2FeSbO_6, such a deviation is noticeable at 50 K. Both compounds' curves are within the spin-liquid regime. For Zn_2FeSbO_6, the data at $T = 5, 10,$ and 20 K show narrow hysteresis loops with coercive fields H_C of approximately 280, 20, and 7 Oe, respectively (inset of Figure 8a). In contrast, for Zn_2MnSbO_6, a coercive field of about 280 Oe is observed in the data only at $T = 2$ K (inset of Figure 8b). This further corroborates the spin-glass
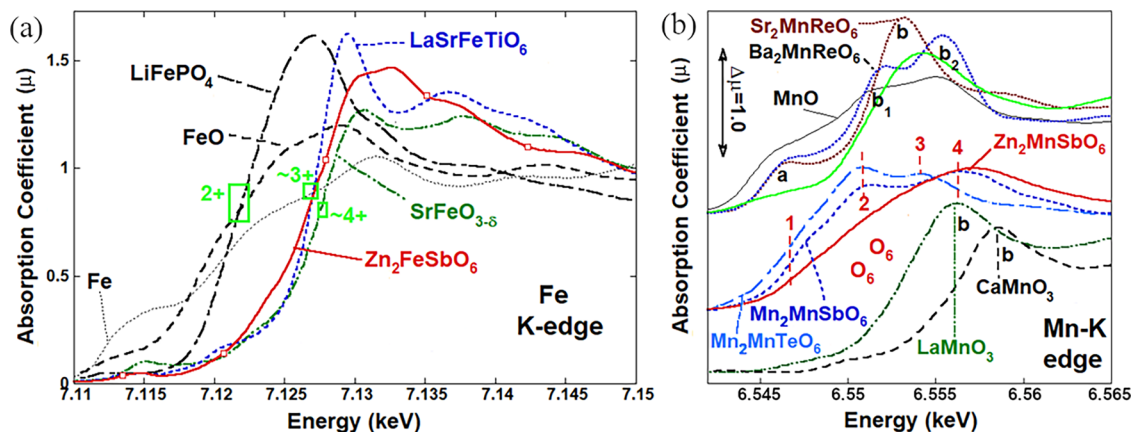
Figure 9. (a) Fe K-edge for Zn_2FeSbO_6 (solid red) and various standards representative of both Fe^{2+} and Fe^{3+} cations ($Fe^{2+}O$, $LiFe^{2+}PO_4$, $LaSrFe^{3+}TiO_6$, and $SrFe^{4+}O_{3-\delta}$) for comparison. Note the chemical shift in the steeply rising portion of the edge between the 2+, 3+, and 4+ standard compounds. The chemical shift of the Zn_2FeSbO_6 compound is consistent with a Fe^{3+} assignment. (b) Mn K-edge of Zn_2MnSbO_6 (solid red) compared to those of several standards representative of the various Mn oxidation states ($Mn^{2+}O$, $Ba_2Mn^{2+}ReO_6$, $Sr_2Mn^{2+}ReO_6$, $LaMn^{3+}O_3$, and $CaMn^{4+}O_3$). The decrease in spectral intensity/features in the 1−3 portion of the spectra, along with the appearance of the absolute 4-peak feature between $Mn^{2+}_2Mn^{2+}TeO_6$ and $Mn^{2+}_2Mn^{3+}SbO_6$ standards, should be noted. The further decrease in the 1−3 range and the 4-peak enhancement underscores the Mn^{3+} character of Zn_2MnSbO_6.

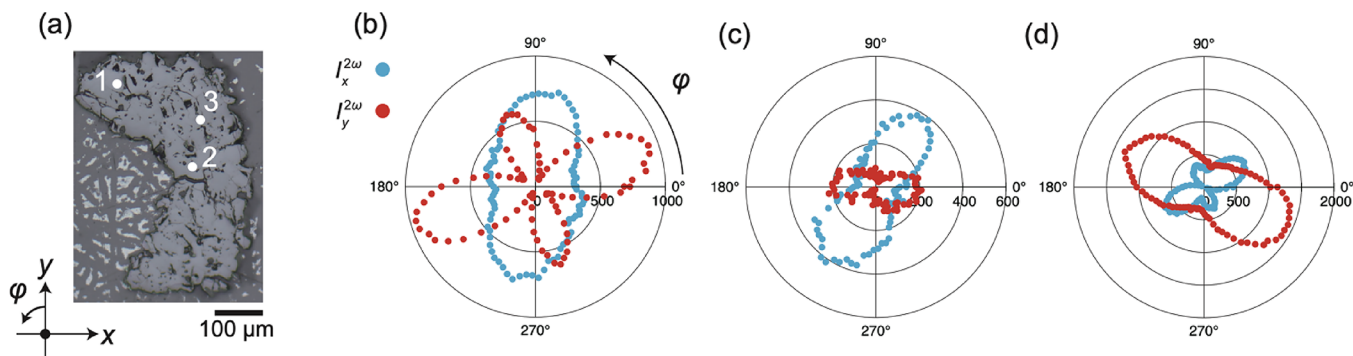**Figure 10.** (a) Optical image of Zn_2MnSbO_6 sample embedded in an epoxy matrix and polished. SHG intensity (radial axis in arbitrary units) as a function of incident polarization angle φ (angular axis) collected from spot (b) 1, (c) 2, and (d) 3. The x- and y-polarized SHG intensities ($I_x^{2\omega}$ and $I_y^{2\omega}$) are represented by blue and red, respectively.

behavior of these two materials, as spin glasses typically show minimal or no hysteresis due to their magnetic moments being frozen in random orientations, inhibiting the formation of coherent magnetic domains. A comparison of the magnetic moment per formula unit versus the applied field for Zn_2FeSbO_6 and Zn_2MnSbO_6 at $T = 5$ K is shown in Figure S11. There is a clear difference in the magnetic responses of these two systems. Zn_2FeSbO_6 exhibits a steeper increase in magnetization with increasing field, reaching a larger magnetic moment per formula unit at high fields. This behavior indicates that the spins for the Fe compound undergo greater alignment under the applied field. In contrast, Zn_2MnSbO_6 shows a more gradual rise in magnetization with a significantly lower magnetic moment at comparable field strengths, reflecting stronger frustration and a greater degree of spin disorder. This difference in the slope and magnitude of the $M(H)$ curves further corroborates that the magnetic frustration in Zn_2MnSbO_6 is more pronounced than that in Zn_2FeSbO_6, preventing the spins from aligning as readily with the external field.

The electrical resistivity of both compounds is too insulating and out of the measurable range of the PPMS.

3.4. X-ray Absorption Near-Edge Spectroscopy. To investigate the oxidation states of Fe and Mn in Zn_2FeSbO_6

and Zn_2MnSbO_6, the XANES Fe K-edges and Mn K-edges were measured. XANES measurements of the K-edges of $3d$ row transition metals are extremely useful to probe the transition metal valence and electronic configuration. The K near edges of $3d$ transition compounds are dominated by $1s$ to $4p$ transition peak features, which typically exhibit a chemical shift toward higher energy with increasing the valence of the $3d$ element. In Figure 9a, the Fe−K main edge for Zn_2FeSbO_6 is compared to the spectra for the standards containing several Fe oxidation states: Fe^0, $Fe^{2+}O$, $LiFe^{2+}PO_4$, $LaSrFe^{3+}TiO_6$, and $SrFe^{4+}O_{3-\delta}$.[98,99] The main edge for Zn_2FeSbO_6 is chemically shifted to higher energy than those for Fe^{2+} standards FeO and $LiFePO_4$. Moreover, the energies of the steeply rising portion and peak of the Zn_2FeSbO_6 spectrum is a Fe^{3+} state assignment in Zn_2FeSbO_6. In Figure 9b, the main edge for Zn_2MnSbO_6 is compared with the spectra for the standards $Mn^{2+}O$, $LaMn^{3+}O_3$, and $CaMn^{4+}O_3$[88,100] and other compounds $Mn_2Mn^{2+}TeO_6$ Mn_3SbO_6, $Ba_2Mn^{2+}ReO_6$, and $Sr_2Mn^{2+}ReO_6$.[20,72,101] As noted in the figure caption, the spectral steeply rising portion at the edge onset and the peak energy location of the Zn_2MnSbO_6 spectrum support a Mn^{3+} state for Mn in this compound.

3.5. Second Harmonic Generation (SHG). SHG measurement was utilized for the final space group assignation

of Zn_2MnSbO_6. According to the equation $P_i = d_{ijk}E_jE_k$,[101] where P_i is the second-order induced polarization and E_j (and E_k) is the electric field of the incident light, SHG measurements probe a third-rank polar tensor, d_{ijk}, which has nonzero components only when the crystal belongs to a NCS point group. Thus, only materials with NCS crystal structures exhibit an SHG response, through which doubled-frequency and halved-wavelength light can be detected. The x- and y-polarized 400 nm SHG intensity collected from three different spots (Figure 10a) of the Zn_2MnSbO_6 sample are plotted in Figure 10b10d as a function of the polarization angle (φ) of the fundamental 800 nm light. We observed a finite SHG signal from all the spots, corroborating the NCS structure of Zn_2MnSbO_6, i.e., the P-NCS $R3$ space group (no. 146) in this case. SHG polar plots of polycrystalline samples are isotropic and show no φ-dependence, but those from the Zn_2MnSbO_6 sample exhibit anisotropy, indicating the single-crystalline nature of each spot. However, the piece consists of multiple domains, as seen from the variation of the polar plot shape from spot to spot (Figure 10b−d).

4. CONCLUSIONS

We have successfully synthesized two new transition metal polar corundum derivatives, Zn_2FeSbO_6 and Zn_2MnSbO_6, by a high-pressure and high-temperature technique and have characterized them by SEM/EDS, XANES, SHG, PPMS (magnetization), and bulk powder and single-crystal XRD. XANES spectroscopy revealed the oxidation states as Fe^{3+} for Zn_2FeSbO_6 and Mn^{3+} for Zn_2MnSbO_6. The magnetic properties indicate spin-glass behavior with antiferromagnetic interactions in both compounds, with Zn_2FeSbO_6 exhibiting a T_N = 9 K, while Zn_2MnSbO_6 showing a magnetic ordering at approximately 4 K. Both compounds show magnetic frustration, which is more than twice as strong in the Mn compound. SHG measurements confirmed the noncentrosymmetric nature of Zn_2MnSbO_6, with $R3$ space group symmetry.

The atomic coordinates, occupancies, and atomic displacement parameters of all atoms in the two crystal structures were determined by single-crystal and high-resolution (0.4 Å) X-ray data (Mo Kα). In Zn_2FeSbO_6, a split cation site is occupied by 68% Zn at (0 0 0.7147) and 32% Fe at (0 0 0.7037), and its face-sharing neighboring cation is also split with 68% Fe at (0 0 0.4982) and 32% Zn at (0 0 0.4869). The two remaining cation sites (0 0 0.2) and (0 0 0) were found to be fully occupied by Zn and Sb, respectively. Thus, our model for Zn_2FeSbO_6 consists of a cocrystal of superimposed NTO and OIL components with a ratio of approximately 2:1. In Zn_2MnSbO_6, we observed a significantly different site mixing motif, where all sites are split and the (0 0 0.7) site was found to be occupied by 84% Mn and 16% Sb and the (0 0 0) site contained 16% Mn and 84% Sb. The (0 0 0.5) and (0 0 0.2) sites were found to also be split and occupied by only Zn. Thus, for our model of Zn_2MnSbO_6, a crystal with two nearly identical, but noncrystallographically related, OIL components in a ratio of approximately 5:1, was obtained. The approximate 2:1 and 5:1 ratio values obtained here do not appear to have any correlation to the crystallography of these crystals and may have an electronic and/or magnetic basis. The derived level of precision of the structure analyses is good despite the two models having multiple components resulting from merohedral twinning and cocrystallization. The use of anisotropic displacement parameters for all atoms enhances the precision and accuracy of the determination of the positions and

compositions of the cation sites. Based upon comparisons of octahedral volumes, distortion indices, and elongation parameters for cation sites, the most distorted cation octahedron for both Zn_2FeSbO_6, and Zn_2MnSbO_6 is that for the minor Zn^{2+} component in the (0 0 0.5) site. In Zn_2FeSbO_6, an unexpected site mixing of Fe^{3+} with Zn^{2+} rather than Fe^{3+} with Sb^{5+} is accompanied by significant distortions of octahedral geometries for these face-sharing minor component cations. In Zn_2MnSbO_6, the expected site mixing of Mn^{3+} with Sb^{5+} is observed between corner-sharing octahedra, rather than between closer face-sharing octahedra as in Zn_2FeSbO_6. Despite Fe^{3+} and Mn^{3+} having the same effective ionic radius, the sum of separations between octahedra along the z-axis in Zn_2FeSbO_6 is shorter than those in Zn_2MnSbO_6, resulting in a larger unit cell volume for the latter, despite the higher formal molecular weight of the former.

These findings not only enhance our understanding of the structural and magnetic complexities in transition metal polar corundum derivative phases but also open avenues for exploring their potential applications in multifunctional materials.

■ ASSOCIATED CONTENT

ⓢ Supporting Information

The Supporting Information is available free of charge at https://pubs.acs.org/doi/10.1021/acs.chemmater.4c02146.

Initial-stage atomic coordinates and equivalent isotropic displacement parameters adopted in solving the two structures; anisotropic displacement parameters for both Zn_2FeSbO_6 and Zn_2MnSbO_6; bond distances and angles; nearest cation···cation distances orthogonal to the c-axis and sequential cation···cation distances along the c-axis for both compounds; atomic coordinates from Rietveld refinement and corresponding Rietveld refinement profiles and results for Zn_2FeSbO_6 and Zn_2MnSbO_6; precession images of the $0kl$, $h0l$, and $hk0$ reflection zones for both compounds; light optical microscopy and SEM images showing the microstructures of both compounds; coordination geometry of cations in Zn_2FeSbO_6 and Zn_2MnSbO_6; inverse magnetic susceptibilities, including Curie−Weiss fits, for both compounds; isothermal magnetizations at T = 5 K for both Zn_2FeSbO_6 and Zn_2MnSbO_6 (PDF)

■ AUTHOR INFORMATION

Corresponding Author

Martha Greenblatt − *Department of Chemistry and Chemical Biology, Rutgers, The State University of New Jersey, Piscataway, New Jersey 08854, United States;* ⓞ orcid.org/0000-0002-1806-2766; Email: greenbla@chem.rutgers.edu

Authors

Alessia Provino − *Department of Chemistry and Chemical Biology, Rutgers, The State University of New Jersey, Piscataway, New Jersey 08854, United States;* Present Address: Department of Material Sciences and Engineering, Alfred University, Alfred, New York 14802, United States; ⓞ orcid.org/0000-0002-7577-6642

Thomas J. Emge − *Department of Chemistry and Chemical Biology, Rutgers, The State University of New Jersey,*

Piscataway, New Jersey 08854, United States; ● orcid.org/
0000-0002-5307-7250

David Walker − *Lamont-Doherty Earth Observatory,
Columbia University, Palisades, New York 10964, United
States*

Corey E. Frank − *Department of Chemistry and Chemical
Biology, Rutgers, The State University of New Jersey,
Piscataway, New Jersey 08854, United States;* Present
Address: Department of Physics, University of Maryland,
College Park, Maryland 20742, United States;
● orcid.org/0000-0003-2638-7795

Suguru Yoshida − *Department of Materials Science and
Engineering, Pennsylvania State University, University Park,
Pennsylvania 16802, United States;* ● orcid.org/0000-
0002-1016-5031

Venkatraman Gopalan − *Department of Materials Science
and Engineering, Pennsylvania State University, University
Park, Pennsylvania 16802, United States*

Mark Croft − *Department of Physics & Astronomy, Rutgers,
The State University of New Jersey, Piscataway, New Jersey
08854, United States*

Zheng Deng − *Beijing National Laboratory for Condensed
Matter Physics, Institute of Physics, Chinese Academy of
Sciences, Beijing 100190, China*

Changqing Jin − *Beijing National Laboratory for Condensed
Matter Physics, Institute of Physics, Chinese Academy of
Sciences, Beijing 100190, China*

Pietro Manfrinetti − *Department of Chemistry, University of
Genoa, Genoa 16146, Italy; Institute SPIN-CNR, Genoa
16152, Italy;* ● orcid.org/0000-0002-3346-5619

Complete contact information is available at:
https://pubs.acs.org/10.1021/acs.chemmater.4c02146

Notes
The authors declare no competing financial interest.

■ DEDICATION

In memory of Prof. Francis J. DiSalvo.

■ REFERENCES

(1) De Teresa, J. M.; Serrate, D.; Blasco, J.; Ibarra, M. R.; Morellon, L. Impact of Cation Size on Magnetic Properties of (A A′)$_2$FeReO$_6$ Double Perovskites. *Phys. Rev. B* **2004**, *69* (14), No. 144401.

(2) Fisher, B.; Genossar, J.; Chashka, K. B.; Knizhnik, A.; Patlagan, L.; Reisner, G. M. Variable Range Hopping in A$_2$MnReO$_6$ (A = Ca, Sr, Ba). *J. Appl. Phys.* **2008**, *104* (3), No. 033716.

(3) Kato, H.; Okuda, T.; Okimoto, Y.; Tomioka, Y.; Oikawa, K.; Kamiyama, T.; Tokura, Y. Structural and Electronic Properties of the Ordered Double Perovskites A$_2$MReO$_6$ (A = Sr,Ca; M = Mg,Sc,Cr,Mn,Fe,Co,Ni,Zn). *Phys. Rev. B* **2004**, *69* (18), No. 184412.

(4) Kobayashi, K.-I.; Kimura, T.; Sawada, H.; Terakura, K.; Tokura, Y. Room-Temperature Magnetoresistance in an Oxide Material with an Ordered Double-Perovskite Structure. *Nature* **1998**, *395* (6703), 677−680.

(5) Serrate, D.; De Teresa, J. M.; Algarabel, P. A.; Marquina, C.; Blasco, J.; Ibarra, M. R.; Galibert, J. Magnetoelastic Coupling in Sr$_2$(Fe$_{1−x}$Cr$_x$)ReO$_6$ Double Perovskites. *J. Phys.: Condens. Matter* **2007**, *19* (43), No. 436226.

(6) Sikora, M.; Kapusta, Cz; Borowiec, M.; Oates, C. J.; Prochazka, V.; Rybicki, D.; Zajac, D.; De Teresa, J. M.; Marquina, C.; Ibarra, M. R. Evidence of Unquenched Re Orbital Magnetic Moment in AA′FeReO$_6$ Double Perovskites. *Appl. Phys. Lett.* **2006**, *89* (6), No. 062509.

(7) Vasala, S.; Karppinen, M. A$_2$B′B″O$_6$ Perovskites: A Review. *Prog. Solid State Chem.* **2015**, *43* (1−2), 1−36.

(8) Retuerto, M.; Jiménez-Villacorta, F.; Martínez-Lope, M. J.; Huttel, Y.; Roman, E.; Fernández-Díaz, M. T.; Alonso, J. A. Study of the Valence State and Electronic Structure in Sr$_2$FeMO$_6$ (M = W, Mo, Re and Sb) Double Perovskites. *Phys. Chem. Chem. Phys.* **2010**, *12* (41), 13616.

(9) Paul, A. K.; Jansen, M.; Yan, B.; Felser, C.; Reehuis, M.; Abdala, P. M. Synthesis, Crystal Structure, and Physical Properties of Sr$_2$FeOsO$_6$. *Inorg. Chem.* **2013**, *52* (11), 6713−6719.

(10) Kobayashi, K.-I.; Kimura, T.; Tomioka, Y.; Sawada, H.; Terakura, K.; Tokura, Y. Intergrain Tunneling Magnetoresistance in Polycrystals of the Ordered Double Perovskite Sr$_2$FeReO$_6$. *Phys. Rev. B* **1999**, *59* (17), 11159−11162.

(11) King, G.; Woodward, P. M. Cation Ordering in Perovskites. *J. Mater. Chem.* **2010**, *20* (28), 5785.

(12) Yin, W.-J.; Weng, B.; Ge, J.; Sun, Q.; Li, Z.; Yan, Y. Oxide Perovskites, Double Perovskites and Derivatives for Electrocatalysis, Photocatalysis, and Photovoltaics. *Energy Environ. Sci.* **2019**, *12* (2), 442−462.

(13) Li, M.-R.; Walker, D.; Retuerto, M.; Sarkar, T.; Hadermann, J.; Stephens, P. W.; Croft, M.; Ignatov, A.; Grams, C. P.; Hemberger, J.; Nowik, I.; Halasyamani, P. S.; Tran, T. T.; Mukherjee, S.; Dasgupta, T. S.; Greenblatt, M. Polar and Magnetic Mn$_2$FeMO$_6$ (M = Nb, Ta) with LiNbO$_3$-Type Structure - High Pressure Synthesis. *Angew. Chem. Int. Ed* **2013**, *52*, 8406−8410.

(14) Li, M.; Croft, M.; Stephens, P. W.; Ye, M.; Vanderbilt, D.; Retuerto, M.; Deng, Z.; Grams, C. P.; Hemberger, J.; Hadermann, J.; Li, W.; Jin, C.; Saouma, F. O.; Jang, J. I.; Akamatsu, H.; Gopalan, V.; Walker, D.; Greenblatt, M. Mn$_2$FeWO$_6$: A New Ni$_3$TeO$_6$-Type Polar and Magnetic Oxide. *Adv. Mater.* **2015**, *27* (13), 2177−2181.

(15) Li, M.; Retuerto, M.; Stephens, P. W.; Croft, M.; Sheptyakov, D.; Pomjakushin, V.; Deng, Z.; Akamatsu, H.; Gopalan, V.; Sánchez-Benítez, J.; Saouma, F. O.; Jang, J. I.; Walker, D.; Greenblatt, M. Low-Temperature Cationic Rearrangement in a Bulk Metal Oxide. *Angew. Chem. Int. Ed* **2016**, *55* (34), 9862−9867.

(16) Kim, S. W.; Deng, Z.; Fischer, Z.; Lapidus, S. H.; Stephens, P. W.; Li, M.-R.; Greenblatt, M. Structure and Magnetic Behavior of Layered Honeycomb Tellurates, BiM(III)TeO$_6$ (M = Cr, Mn, Fe). *Inorg. Chem.* **2016**, *55* (20), 10229−10237.

(17) Frank, C. E.; McCabe, E. E.; Orlandi, F.; Manuel, P.; Tan, X.; Deng, Z.; Croft, M.; Cascos, V.; Emge, T.; Feng, H. L.; Lapidus, S.; Jin, C.; Wu, M.; Li, M. R.; Ehrlich, S.; Khalid, S.; Quackenbush, N.; Yu, S.; Walker, D.; Greenblatt, M. Mn$_2$CoReO$_6$: A Robust Multisublattice Antiferromagnetic Perovskite with Small A-Site Cations. *Chem. Commun.* **2019**, *55* (23), 3331−3334.

(18) Feng, H. L.; Deng, Z.; Croft, M.; Lapidus, S. H.; Zu, R.; Gopalan, V.; Grams, C. P.; Hemberger, J.; Liu, S.; Tyson, T. A.; Frank, C. E.; Jin, C.; Walker, D.; Greenblatt, M. High-Pressure Synthesis and Ferrimagnetism of Ni$_3$TeO$_6$-Type Mn$_2$ScMO$_6$ (M = Nb, Ta). *Inorg. Chem.* **2019**, *58* (23), 15953−15961.

(19) Han, Y.; Zeng, Y.; Hendrickx, M.; Hadermann, J.; Stephens, P. W.; Zhu, C.; Grams, C. P.; Hemberger, J.; Frank, C.; Li, S.; Wu, M.; Retuerto, M.; Croft, M.; Walker, D.; Yao, D.-X.; Greenblatt, M.; Li, M.-R. Universal A-Cation Splitting in LiNbO$_3$-Type Structure Driven by Intrapositional Multivalent Coupling. *J. Am. Chem. Soc.* **2020**, *142* (15), 7168−7178.

(20) Feng, H. L.; Kang, C.-J.; Kim, B.; Kim, K.; Croft, M.; Liu, S.; Tyson, T. A.; Stavitski, E.; Zu, R.; Gopalan, V.; Lapidus, S. H.; Frank, C. E.; Shi, Y.; Walker, D.; Greenblatt, M. A Polar Magnetic and Insulating Double Corundum Oxide: Mn_2MnSbO_6 with Ordered Mn(II) and Mn(III) Ions. Chem. Mater. 2021, 33 (16), 6522–6529.

(21) Zhao, S.; Yang, J.-J.; Han, Y.-F.; Wu, M.-X.; Croft, M.; Stephens, P. W.; Walker, D.; Greenblatt, M.; Li, M.-R. High-Pressure Synthesis of Polar and Antiferromagnetic Mn_2MnMoO_6. Chem. Mater. 2022, 34 (4), 1930–1936.

(22) Frank, C. E.; McCabe, E. E.; Orlandi, F.; Manuel, P.; Tan, X.; Deng, Z.; Jin, C.; Croft, M.; Emge, T.; Yu, S.; Wang, H.; Gopalan, V.; Lapidus, S.; Wu, M.; Li, M.-R.; Gross, J.; Burger, P.; Mielewczyk-Gryń, A.; Klimczuk, T.; Xie, W.; Walker, D.; Greenblatt, M. $Fe_{3-x}InSn_xO_6$ (x = 0, 0.25, or 0.5): A Family of Corundum Derivatives with Sn-Induced Polarization and Above Room Temperature Antiferromagnetic Ordering. Chem. Mater. 2022, 34 (11), 5020–5029.

(23) Mathieu, R.; Ivanov, S. A.; Bazuev, G. V.; Hudl, M.; Lazor, P.; Solovyev, I. V.; Nordblad, P. Magnetic Order near 270 K in Mineral and Synthetic Mn_2FeSbO_6 Ilmenite. Appl. Phys. Lett. 2011, 98 (20), No. 202505.

(24) Goldschmidt, V. M. Die Gesetze der Krystallochemie. Naturwissenschaften 1926, 14 (21), 477–485.

(25) Woodward, P. M.; Sleight, A. W.; Du, L.-S.; Grey, C. P. Structural Studies and Order−Disorder Phenomenon in a Series of New Quaternary Tellurates of the Type $A^{2+}_2M^{4+}Te^{6+}O_6$ and $A^{1+}_2M^{4+}Te^{6+}O_6$. J. Solid State Chem. 1999, 147 (1), 99–116.

(26) Hoel, C. A.; Amores, J. M. G.; Morán, E.; Alario-Franco, M. A.; Gaillard, J.-F.; Poeppelmeier, K. R. High-Pressure Synthesis and Local Structure of Corundum-Type $In_{2-2x}Zn_xSn_xO_3$ ($x \leq 0.7$). J. Am. Chem. Soc. 2010, 132 (46), 16479–16487.

(27) Choisnet, J.; Rulmont, A.; Tarte, P. Les tellurates mixtes Li_2ZrTeO_6 et Li_2HfTeO_6: un nouveau phénomène d'ordre dans la famille corindon. J. Solid State Chem. 1988, 75 (1), 124–135.

(28) Li, M.; Retuerto, M.; Walker, D.; Sarkar, T.; Stephens, P. W.; Mukherjee, S.; Dasgupta, T. S.; Hodges, J. P.; Croft, M.; Grams, C. P.; Hemberger, J.; Sánchez-Benítez, J.; Huq, A.; Saouma, F. O.; Jang, J. I.; Greenblatt, M. Magnetic-Structure-Stabilized Polarization in an Above-Room-Temperature Ferrimagnet. Angew. Chem. 2014, 126 (40), 10950–10954.

(29) Oh, Y. S.; Artyukhin, S.; Yang, J. J.; Zapf, V.; Kim, J. W.; Vanderbilt, D.; Cheong, S.-W. Non-Hysteretic Colossal Magneto-electricity in a Collinear Antiferromagnet. Nat. Commun. 2014, 5 (1), 3201.

(30) Ivanov, S. A.; Mathieu, R.; Nordblad, P.; Tellgren, R.; Ritter, C.; Politova, E.; Kaleva, G.; Mosunov, A.; Stefanovich, S.; Weil, M. Spin and Dipole Ordering in Ni_2InSbO_6 and Ni_2ScSbO_6 with Corundum-Related Structure. Chem. Mater. 2013, 25 (6), 935–945.

(31) Arévalo-López, A. M.; McNally, G. M.; Attfield, J. P. Large Magnetization and Frustration Switching of Magnetoresistance in the Double-Perovskite Ferrimagnet Mn_2FeReO_6. Angew. Chem. Int. Ed 2015, 54 (41), 12074–12077.

(32) Kato, H.; Okuda, T.; Okimoto, Y.; Tomioka, Y.; Takenoya, Y.; Ohkubo, A.; Kawasaki, M.; Tokura, Y. Metallic Ordered Double-Perovskite Sr_2CrReO_6 with Maximal Curie Temperature of 635 K. Appl. Phys. Lett. 2002, 81 (2), 328–330.

(33) Kim, T. H.; Uehara, M.; Cheong, S.-W.; Lee, S. Large Room-Temperature Intergrain Magnetoresistance in Double Perovskite $SrFe_{1-x}(Mo \text{ or } Re)_xO_3$. Appl. Phys. Lett. 1999, 74 (12), 1737–1739.

(34) Retuerto, M.; Li, M.-R.; Stephens, P. W.; Sánchez-Benítez, J.; Deng, X.; Kotliar, G.; Croft, M. C.; Ignatov, A.; Walker, D.; Greenblatt, M. Half-Metallicity in Pb_2CoReO_6 Double Perovskite and High Magnetic Ordering Temperature in Pb_2CrReO_6 Perovskite. Chem. Mater. 2015, 27 (12), 4450–4458.

(35) Li, M.; Retuerto, M.; Deng, Z.; Stephens, P. W.; Croft, M.; Huang, Q.; Wu, H.; Deng, X.; Kotliar, G.; Sánchez-Benítez, J.; Hadermann, J.; Walker, D.; Greenblatt, M. Giant Magnetoresistance in the Half-Metallic Double-Perovskite Ferrimagnet Mn_2FeReO_6. Angew. Chem. Int. Ed 2015, 54 (41), 12069–12073.

(36) Li, M.-R.; Hodges, J. P.; Retuerto, M.; Deng, Z.; Stephens, P. W.; Croft, M. C.; Deng, X.; Kotliar, G.; Sánchez-Benítez, J.; Walker, D.; Greenblatt, M. Mn_2MnReO_6: Synthesis and Magnetic Structure Determination of a New Transition-Metal-Only Double Perovskite Canted Antiferromagnet. Chem. Mater. 2016, 28 (9), 3148–3158.

(37) Krockenberger, Y.; Mogare, K.; Reehuis, M.; Tovar, M.; Jansen, M.; Vaitheeswaran, G.; Kanchana, V.; Bultmark, F.; Delin, A.; Wilhelm, F.; Rogalev, A.; Winkler, A.; Alff, L. Sr_2CrOsO_6: End Point of a Spin-Polarized Metal-Insulator Transition by 5 d Band Filling. Phys. Rev. B 2007, 75 (2), No. 020404.

(38) Samanta, K.; Sanyal, P.; Saha-Dasgupta, T. Half-Metallic Behavior in Doped Sr_2CrOsO_6 Double Perovskite with High Transition Temperature. Sci. Rep 2015, 5 (1), 15010.

(39) Feng, H. L.; Arai, M.; Matsushita, Y.; Tsujimoto, Y.; Guo, Y.; Sathish, C. I.; Wang, X.; Yuan, Y.-H.; Tanaka, M.; Yamaura, K. High-Temperature Ferrimagnetism Driven by Lattice Distortion in Double Perovskite Ca_2FeOsO_6. J. Am. Chem. Soc. 2014, 136 (9), 3326–3329.

(40) Feng, H. L.; Calder, S.; Ghimire, M. P.; Yuan, Y.-H.; Shirako, Y.; Tsujimoto, Y.; Matsushita, Y.; Hu, Z.; Kuo, C.-Y.; Tjeng, L. H.; Pi, T.-W.; Soo, Y.-L.; He, J.; Tanaka, M.; Katsuya, Y.; Richter, M.; Yamaura, K. Ba_2NiOsO_6: A Dirac-Mott Insulator with Ferromagnetism near 100 K. Phys. Rev. B 2016, 94 (23), No. 235158.

(41) Feng, H. L.; Adler, P.; Reehuis, M.; Schnelle, W.; Pattison, P.; Hoser, A.; Felser, C.; Jansen, M. High-Temperature Ferrimagnetism with Large Coercivity and Exchange Bias in the Partially Ordered 3d/5d Hexagonal Perovskite $Ba_2Fe_{1.12}Os_{0.88}O_6$. Chem. Mater. 2017, 29 (2), 886–895.

(42) Goodenough, J. B. Perspective on Engineering Transition-Metal Oxides. Chem. Mater. 2014, 26 (1), 820–829.

(43) Li, M.-R.; Stephens, P. W.; Croft, M.; Deng, Z.; Li, W.; Jin, C.; Retuerto, M.; Hodges, J. P.; Frank, C. E.; Wu, M.; Walker, D.; Greenblatt, M. $Mn_2(Fe_{0.8}Mo_{0.2})MoO_6$: A Double Perovskite with Multiple Transition Metal Sublattice Magnetic Effects. Chem. Mater. 2018, 30 (14), 4508–4514.

(44) Bazuev, G. V.; Golovkin, B. G.; Lukin, N. V.; Kadyrova, N. I.; Zainulin, Yu. G. High Pressure Synthesis and Polymorphism of Complex Oxides Mn_2BSbO_6(B= Fe, V, Cr, Ga, Al). J. Solid State Chem. 1996, 124 (2), 333–337.

(45) Mathieu, R.; Ivanov, S. A.; Solovyev, I. V.; Bazuev, G. V.; Anil Kumar, P.; Lazor, P.; Nordblad, P. Mn_2FeSbO_6: A Ferrimagnetic Ilmenite and an Antiferromagnetic Perovskite. Phys. Rev. B 2013, 87 (1), No. 014408.

(46) Li, M.-R.; Stephens, P. W.; Retuerto, M.; Sarkar, T.; Grams, C. P.; Hemberger, J.; Croft, M. C.; Walker, D.; Greenblatt, M. Designing Polar and Magnetic Oxides: Zn_2FeTaO_6 - in Search of Multiferroics. J. Am. Chem. Soc. 2014, 136 (24), 8508–8511.

(47) Wang, P. S.; Ren, W.; Bellaiche, L.; Xiang, H. J. Predicting a Ferrimagnetic Phase of Zn_2FeOsO_6 with Strong Magnetoelectric Coupling. Phys. Rev. Lett. 2015, 114 (14), No. 147204.

(48) Li, M.-R.; McCabe, E. E.; Stephens, P. W.; Croft, M.; Collins, L.; Kalinin, S. V.; Deng, Z.; Retuerto, M.; Sen Gupta, A.; Padmanabhan, H.; Gopalan, V.; Grams, C. P.; Hemberger, J.; Orlandi, F.; Manuel, P.; Li, W.-M.; Jin, C.-Q.; Walker, D.; Greenblatt, M. Magnetostriction-Polarization Coupling in Multiferroic Mn_2MnWO_6. Nat. Commun. 2017, 8 (1), 2037.

(49) Ji, K.; Solana-Madruga, E.; Arevalo-Lopez, A. M.; Manuel, P.; Ritter, C.; Senyshyn, A.; Attfield, J. P. Lock-in Spin Structures and Ferrimagnetism in Polar $Ni_{2-x}Co_xScSbO_6$ Oxides. Chem. Commun. 2018, 54 (88), 12523–12526.

(50) Solana-Madruga, E.; Aguilar-Maldonado, C.; Ritter, C.; Huvé, M.; Mentré, O.; Attfield, J. P.; Arévalo-López, Á. M. Complex Magnetism in Ni_3TeO_6 -Type Co_3TeO_6 and High-Pressure Polymorphs of $Mn_{3-x}Co_xTeO_6$ Solid Solutions. Chem. Commun. 2021, 57 (20), 2511–2514.

(51) Skiadopoulou, S.; Retuerto, M.; Borodavka, F.; Kadlec, C.; Kadlec, F.; Míšek, M.; Prokleška, J.; Deng, Z.; Tan, X.; Frank, C.; Alonso, J. A.; Fernandez-Diaz, M. T.; Croft, M.; Orlandi, F.; Manuel, P.; McCabe, E.; Legut, D.; Greenblatt, M.; Kamba, S. Structural, Magnetic, and Spin Dynamical Properties of the Polar Antiferro-

magnets Ni$_{3-x}$Co$_x$TeO$_6$ (x = 1, 2). *Phys. Rev. B* **2020**, *101* (1), No. 014429.

(52) Selb, E.; Buttlar, T.; Janka, O.; Tribus, M.; Ebbinghaus, S. G.; Heymann, G. Multianvil High-Pressure/High-Temperature Synthesis and Characterization of Magnetoelectric HP-Co $_3$TeO$_6$. *J. Mater. Chem. C* **2021**, *9* (16), 5486−5496.

(53) De, C.; Arévalo-López, Á. M.; Orlandi, F.; Manuel, P.; Attfield, J. P.; Sundaresan, A. Isovalent Cation Ordering in the Polar Rhombohedral Perovskite Bi$_2$FeAlO$_6$. *Angew. Chem. Int. Ed* **2018**, *57* (49), 16099−16103.

(54) Swaffer, M.; Slater, P. R.; Gover, R. K. B.; Matsumura, T.; Kanno, R.; Kamiyama, T. La$_2$MgGeO$_6$: A Novel Ge Based Perovskite Synthesised under Ambient Pressure. *Chem. Commun.* **2002**, *16*, 1776−1777.

(55) Archaimbault, F.; Choisnet, J.; Rulmont, A.; Tarte, P. Lithium Defect and Ordering Phenomena in the New LiNbO$_3$ like Mixed Tellurates: Li$_{2-x}$(Zr^{4+},Nb^{5+},Te^{6+})$_2$O$_6$ (X⩽0.5). *Mater. Chem. Phys.* **1992**, *30* (4), 245−252.

(56) Zhao, M.-H.; Wang, W.; Han, Y.; Xu, X.; Sheng, Z.; Wang, Y.; Wu, M.; Grams, C. P.; Hemberger, J.; Walker, D.; Greenblatt, M.; Li, M.-R. Reversible Structural Transformation between Polar Polymorphs of Li$_2$GeTeO$_6$. *Inorg. Chem.* **2019**, *58* (2), 1599−1606.

(57) Lu, W.; Gao, Z.; Liu, X.; Tian, X.; Wu, Q.; Li, C.; Sun, Y.; Liu, Y.; Tao, X. Rational Design of a LiNbO$_3$ -like Nonlinear Optical Crystal, Li $_2$ ZrTeO $_6$, with High Laser-Damage Threshold and Wide Mid-IR Transparency Window. *J. Am. Chem. Soc.* **2018**, *140* (40), 13089−13096.

(58) Selb, E.; Declara, L.; Bayarjargal, L.; Podewitz, M.; Tribus, M.; Heymann, G. Crystal Structure and Properties of a UV-Transparent High-Pressure Polymorph of Mg$_3$TeO$_6$ with Second Harmonic Generation Response. *Eur. J. Inorg. Chem.* **2019**, *2019* (43), 4668−4676.

(59) Arévalo-López, Á. M.; Solana-Madruga, E.; Arévalo-López, E. P.; Khalyavin, D.; Kepa, M.; Dos santos-García, A. J.; Sáez-Puche, R.; Attfield, J. P. Evolving Spin Periodicity and Lock-in Transition in the Frustrated Ordered Ilmenite-Type β − Mn$_2$InSbO$_6$. *Phys. Rev. B* **2018**, *98* (21), No. 214403.

(60) Solana-Madruga, E.; Dos Santos-García, A. J.; Arévalo-López, A. M.; Ávila-Brande, D.; Ritter, C.; Attfield, J. P.; Sáez-Puche, R. High Pressure Synthesis of Polar and Non-Polar Cation-Ordered Polymorphs of Mn$_2$ScSbO$_6$. *Dalton Trans.* **2015**, *44* (47), 20441−20448.

(61) Bhim, A.; Gopalakrishnan, J.; Natarajan, S. Exploring the Corundum Structure as a Host for Colored Compounds − Synthesis, Structures, and Optical Studies of (MM′)$_3$TeO$_6$ (M = Mg, Mn, Co, Ni, Zn; M′ = Mg, Mn, Co, Ni, Cu). *Eur. J. Inorg. Chem.* **2018**, *2018* (20−21), 2277−2284.

(62) Kim, J.; Yang, J.; Won, C. J.; Kim, K.; Kim, B.; Obeysekera, D.; Lee, D. W.; Cheong, S.-W. Helical versus Collinear Antiferromagnetic Order Tuned by Magnetic Anisotropy in Polar and Chiral (Ni,Mn)$_3$TeO$_6$. *Phys. Rev. Materials* **2021**, *5* (9), No. 094405.

(63) Weil, M.; Mathieu, R.; Nordblad, P.; Ivanov, S. A. Crystal Growth Experiments in the Systems Ni$_2$MSbO$_6$ (M = Sc, In) Using Chemical Vapour Transport Reactions: Ni$_2$InSbO$_6$ and NiSb$_2$O $_6$ Crystals in the Millimetre Range. *Crystal Research and Technology* **2014**, *49* (2−3), 142−151.

(64) Retuerto, M.; Skiadopoulou, S.; Borodavka, F.; Kadlec, C.; Kadlec, F.; Prokleška, J.; Deng, Z.; Alonso, J. A.; Fernandez-Diaz, M. T.; Saouma, F. O.; Jang, J. I.; Legut, D.; Kamba, S.; Greenblatt, M. Structural and Spectroscopic Properties of the Polar Antiferromagnet Ni$_2$MnTeO$_6$. *Phys. Rev. B* **2018**, *97* (14), No. 144418.

(65) Becker, R.; Berger, H. Reinvestigation of Ni$_3$TeO$_6$. *Acta Crystallogr. E Struct Rep. Online* **2006**, *62* (11), i222−i223.

(66) Newnham, R. E.; Meagher, E. P. Crystal Structure of Ni$_3$TeO$_6$. *Mater. Res. Bull.* **1967**, *2* (5), 549−554.

(67) Panneer Muthuselvam, I.; Saranya, K.; Sankar, R.; Bhowmik, R. N.; Kavitha, L. Experimental Study of Multiple Magnetic Transitions in Micrometer and Nano-Grain Sized Ni$_3$TeO$_6$-Type Oxide. *J. Appl. Phys.* **2020**, *128* (12), No. 123902.

(68) Zhou, X.; Yang, J.; Zhu, C.; Han, Y.; Sun, Z.; Huang, X.; Cao, L.; Wang, J.; Fang, Y.; Wang, K.; Zou, B.; Li, M.-R. Robust Yellow-Violet Pigments Tuned by Site-Selective Manganese Chromophores. *Inorg. Chem.* **2021**, *60* (15), 11579−11590.

(69) *Pearson's Crystal Data: Crystal Structure Database for Inorganic Compounds (on DVD)*, Release 2023/24, ASM International: Materials Park, Ohio, USA.

(70) Herbst-Irmer, R.; Sheldrick, G. M. Refinement of Twinned Structures with *SHELXL* 97. *Acta Crystallogr. B Struct Sci.* **1998**, *54* (4), 443−449.

(71) Herbst-Irmer, R.; Sheldrick, G. M. Refinement of Obverse/Reverse Twins. *Acta Crystallogr. B Struct Sci.* **2002**, *58* (3), 477−481.

(72) Popov, G.; Greenblatt, M.; Croft, M. Large Effects of A -Site Average Cation Size on the Properties of the Double Perovskites Ba$_{2-x}$SrxMnReO$_6$: A d5−d1 System. *Phys. Rev. B* **2003**, *67* (2), No. 024406.

(73) Bera, S.; Saha, A.; Mondal, S.; Biswas, A.; Mallick, S.; Chatterjee, R.; Roy, S. Review of Defect Engineering in Perovskites for Photovoltaic Application. *Mater. Adv.* **2022**, *3* (13), 5234−5247.

(74) Li, M.; Retuerto, M.; Stephens, P. W.; Croft, M.; Sheptyakov, D.; Pomjakushin, V.; Deng, Z.; Akamatsu, H.; Gopalan, V.; Sánchez-Benítez, J.; Saouma, F. O.; Jang, J. I.; Walker, D.; Greenblatt, M. Low-Temperature Cationic Rearrangement in a Bulk Metal Oxide. *Angew. Chem. Int. Ed* **2016**, *55* (34), 9862−9867.

(75) Walker, D.; Li, J. Castable Solid Pressure Media for Multianvil Devices. *Matter and Radiation at Extremes* **2020**, *5* (1), No. 018402.

(76) Walker, D.; Carpenter, M. A.; Hitch, C. M. Some Simplifications to Multianvil Devices for High-Pressure Experiments. *Am. Mineral.* **1990**, *75*, 1020−1028.

(77) Rigaku Oxford Diffraction *CrysAlisPro Software System*, Version 1.171.43.105a, Rigaku Corporation: Wroclaw, Poland, 2019.

(78) *SAINT, APEX4* (2021); Bruker AXS Inc.: Madison, Wisconsin, USA.

(79) Sheldrick, G. M. *Bruker SHELXTL Version 5.1*; Bruker AXS Inc.: Madison, Wisconsin, USA 53719, 1997.

(80) Spek, A. L. Structure Validation in Chemical Crystallography. *Acta Crystallogr. D Biol. Crystallogr.* **2009**, *65* (2), 148−155.

(81) Sheldrick, G. M. Crystal Structure Refinement with *SHELXL*. *Acta Crystallogr. C Struct Chem.* **2015**, *71* (1), 3−8.

(82) Hübschle, C. B.; Sheldrick, G. M.; Dittrich, B. *ShelXle*: A Qt Graphical User Interface for *SHELXL*. *J. Appl. Crystallogr.* **2011**, *44* (6), 1281−1284.

(83) Rodríguez-Carvajal, J. Recent Advances in Magnetic Structure Determination by Neutron Powder Diffraction. *Physica B: Condensed Matter* **1993**, *192* (1−2), 55−69.

(84) Macrae, C. F.; Sovago, I.; Cottrell, S. J.; Galek, P. T. A.; McCabe, P.; Pidcock, E.; Platings, M.; Shields, G. P.; Stevens, J. S.; Towler, M.; Wood, P. A. *Mercury 4.0*: From Visualization to Analysis, Design and Prediction. *J. Appl. Crystallogr.* **2020**, *53* (1), 226−235.

(85) Momma, K.; Izumi, F. *VESTA 3* for Three-Dimensional Visualization of Crystal, Volumetric and Morphology Data. *J. Appl. Crystallogr.* **2011**, *44* (6), 1272−1276.

(86) Gelato, L. M.; Parthé, E. *STRUCTURE TIDY* − a Computer Program to Standardize Crystal Structure Data. *J. Appl. Crystallogr.* **1987**, *20* (2), 139−143.

(87) Brown, I. D. Recent Developments in the Methods and Applications of the Bond Valence Model. *Chem. Rev.* **2009**, *109* (12), 6858−6919.

(88) Croft, M.; Sills, D.; Greenblatt, M.; Lee, C.; Cheong, S.-W.; Ramanujachary, K. V.; Tran, D. Systematic Mn D-Configuration Change in the La$_{1-x}$CaxMnO$_3$ System: A Mn K-Edge XAS Study. *Phys. Rev. B* **1997**, *55* (14), 8726−8732.

(89) Mandal, T. K.; Croft, M.; Hadermann, J.; Van Tendeloo, G.; Stephens, P. W.; Greenblatt, M. La$_2$MnVO$_6$ Double Perovskite: A Structural, Magnetic and X-Ray Absorption Investigation. *J. Mater. Chem.* **2009**, *19* (25), 4382.

(90) Mandal, T. K.; Poltavets, V. V.; Croft, M.; Greenblatt, M. Synthesis, Structure and Magnetic Properties of A$_2$MnB′O$_6$ (A = Ca,

Sr; B′=Sb, Ta) Double Perovskites. *J. Solid State Chem.* **2008**, *181* (9), 2325−2331.

(91) Retuerto, M.; Li, M.-R.; Go, Y. B.; Ignatov, A.; Croft, M.; Ramanujachary, K. V.; Hadermann, J.; Hodges, J. P.; Herber, R. H.; Nowik, I.; Greenblatt, M. Magnetic and Structural Studies of the Multifunctional Material $SrFe_{0.75}Mo_{0.25}O_{3−\delta}$. *Inorg. Chem.* **2012**, *51* (22), 12273−12280.

(92) Veith, G. M.; Greenblatt, M.; Croft, M.; Ramanujachary, K. V.; Hattrick-Simpers, J.; Lofland, S. E.; Nowik, I. Synthesis and Characterization of $Sr_3FeMoO_{6.88}$: An Oxygen-Deficient 2D Analogue of the Double Perovskite Sr_2FeMoO_6. *Chem. Mater.* **2005**, *17* (10), 2562−2567.

(93) Shannon, R. D. Revised Effective Ionic Radii and Systematic Studies of Interatomic Distances in Halides and Chalcogenides. *Acta Cryst. A* **1976**, *32* (5), 751−767.

(94) Greedan, J. E. Geometrically Frustrated Magnetic Materials. *J. Mater. Chem.* **2001**, *11* (1), 37−53.

(95) Joy, P. A.; Kumar, P. S. A.; Date, S. K. The Relationship between Field-Cooled and Zero-Field-Cooled Susceptibilities of Some Ordered Magnetic Systems. *J. Phys.: Condens. Matter* **1998**, *10* (48), 11049−11054.

(96) Buschow, K. H. J.; De Boer, F. R. *Physics of Magnetism and Magnetic Materials*; Springer US: Boston, MA, 2003. .

(97) Balents, L. Spin Liquids in Frustrated Magnets. *Nature* **2010**, *464* (7286), 199−208.

(98) Mandal, T. K.; Abakumov, A. M.; Lobanov, M. V.; Croft, M.; Poltavets, V. V.; Greenblatt, M. Synthesis, Structure, and Magnetic Properties of $SrLaMnSbO_6$: A New *B* -Site Ordered Double Perovskite. *Chem. Mater.* **2008**, *20* (14), 4653−4660.

(99) Tummino, M. L. $SrFeO_3$ Peculiarities and Exploitation in Decontamination Processes and Environmentally-Friendly Energy Applications. *Current Research in Green and Sustainable Chemistry* **2022**, *5*, No. 100339.

(100) Li, M. R.; Retuerto, M.; Go, Y. B.; Emge, T. J.; Croft, M.; Ignatov, A.; Ramanujachary, K. V.; Dachraoui, W.; Hadermann, J.; Tang, M. B.; Zhao, J. T.; Greenblatt, M. Crystal Structure, and Properties of $KSbO_3$-Type $Bi_3Mn_{1.9}Te_{1.1}O_{11}$. *J. Solid State Chem.* **2013**, *197*, 543−549.

(101) Denev, S. A.; Lummen, T. T. A.; Barnes, E.; Kumar, A.; Gopalan, V. Probing Ferroelectrics Using Optical Second Harmonic Generation. *J. Am. Ceram. Soc.* **2011**, *94* (9), 2699−2727.